Biophysical Journal
Article

Biophysical Society

3D Protein Dynamics in the Cell Nucleus

Anand P. Singh,[1] Rémi Galland,[2,3] Megan L. Finch-Edmondson,[1,4] Gianluca Grenci,[1] Jean-Baptiste Sibarita,[2,3] Vincent Studer,[2,3] Virgile Viasnoff,[1,5,6,*] and Timothy E. Saunders[1,5,7,*]

[1]Mechanobiology Institute, National University of Singapore, Singapore; [2]Institut Interdisciplinaire de Neurosciences, University of Bordeaux, France; [3]Centre National de la Recherche Scientifique UMR 5297, University of Bordeaux, France; [4]Department of Physiology, National University of Singapore, Singapore; [5]Department of Biological Sciences, National University of Singapore, Singapore; [6]Centre National de la Recherche Scientifique UMI 3639, Singapore; and [7]Institute for Molecular and Cell Biology, A*Star, Singapore

ABSTRACT The three-dimensional (3D) architecture of the cell nucleus plays an important role in protein dynamics and in regulating gene expression. However, protein dynamics within the 3D nucleus are poorly understood. Here, we present, to our knowledge, a novel combination of 1) single-objective based light-sheet microscopy, 2) photoconvertible proteins, and 3) fluorescence correlation microscopy, to quantitatively measure 3D protein dynamics in the nucleus. We are able to acquire >3400 autocorrelation functions at multiple spatial positions within a nucleus, without significant photobleaching, allowing us to make reliable estimates of diffusion dynamics. Using this tool, we demonstrate spatial heterogeneity in Polymerase II dynamics in live U2OS cells. Further, we provide detailed measurements of human-Yes-associated protein diffusion dynamics in a human gastric cancer epithelial cell line.

INTRODUCTION

The cell nucleus is composed of a dense three-dimensional (3D) architecture, with specialized regions essential for gene expression and regulation, and transcriptional regulators are in continual dynamic exchange between different compartments (1). Many key processes depend on the physical dimensions and spatial organization of the nucleus (2), therefore, quantifying the spatio-temporal protein dynamics in the full 3D nucleus could provide useful information on macromolecule behavior and nuclear organization (3). At present, microscopy methods for quantitative measurement of protein dynamics have restricted sensitivity due to high background and/or potential damage to the live cell from high photon loads. These limitations inhibit an understanding of dynamics in the inherently heterogeneous 3D live cell.

Fluorescence correlation spectroscopy (FCS) is a quantitative method for measuring protein dynamics and binding in live single cells and in vivo (4,5). Recently, there have been two important advances in FCS technology: first, it has been extended from single point to multiplex imaging-FCS via use of light-sheet microscopy (SPIM) (6–9), allowing simultaneous, spatially extended dynamic measurements; and second, the adoption of photoactivatable fluorophores has optimized the relative number of particles in the observation volume, significantly improving the quality of the autocorrelation functions (ACFs), which are central to analysis of FCS data ((5,10), and see the Supporting Material). Furthermore, camera improvements (in both speed and sensitivity) have enabled faster and longer image acquisition times (8,9), and these longer intensity traces can be autocorrelated temporally and spatially to create contiguous maps of diffusivity, concentration, and binding in two dimensions (8,11–15). By being able to record an extended region of space, we can overcome the limitation of point-FCS for which results are highly sensitive to the specific regions imaged.

Extending multiplex imaging FCS to three dimensions requires either simultaneous multiplane illumination and acquisition, or fast sequential multiplane imaging. Simultaneous multiplane imaging systems require multi-light-sheet generation, controlled distance between the imaging planes, and simultaneous focusing of the excited planes on a camera. Multiple light-sheet microscopy (16) enables simultaneous excitation of multiple planes but with a ~5–7 μm thick light-sheet and a fixed distance between planes (10–15 μm). In addition, detection of the multiple excited planes requires moving the sample or objective, leading to a sequential acquisition in practice. Simultaneous multiplane acquisition on a single camera can be achieved using a diffractive

Submitted June 2, 2016, and accepted for publication November 21, 2016.

*Correspondence: virgile.viasnoff@espci.fr or dbsste@nus.edu.sg

Anand P. Singh and Remi Galland contributed equally to this work.

Editor: Paul Wiseman.

http://dx.doi.org/10.1016/j.bpj.2016.11.3196

multifocus grating (17,18); however, the use of wide field excitation schemes currently prevents their use for live multiplane FCS imaging. Sequential single-plane FCS imaging requires moving the sample through the light-sheet plane or adjusting the detection path according to the light-sheet depth into the sample. However, photobleaching typically drastically limits the effective number of planes where imaging FCS can be performed. Thus, multiplane FCS requires specific illumination and detection schemes, as well as labeling strategies limiting photobleaching effects.

Here, we present, to our knowledge, a novel combination of a single-objective based light-sheet microscope (soSPIM) (19) with photoconvertible fluorophores to perform sequential imaging FCS on up to eight planes (<1 μm apart). This enables quantification of protein diffusion effectively across the entire cell nucleus in a multiplexed-multiplane fashion. First, we tested and calibrated the performance of this soSPIM-FCS combination with organic dyes in a buffer solution, which showed similar sensitivity and calibration parameters as previously reported using SPIM setups (8,20). We then tested the sensitivity of soSPIM-FCS by imaging enhanced green fluorescent proteins (eGFP) in live NIH3T3 cells. To explore 3D protein dynamics, we used photoconvertible Dendra2-tagged RNA Polymerase II (Dendra2-Pol II) protein to create multiplexed-multiplane protein diffusion maps that traverse the 3D cell nucleus. We acquired roughly an order of magnitude more correlation functions from a single cell nucleus than previously reported. Importantly, the improvement in the quality of correlation functions and the number of data points per cell was only possible due to the continuous photoconversion of a sparse subset of proteins in the acquisition channel leading to a high FCS signal-to-noise ratio (SNR) and significantly reduced photobleaching effects. Because the total data acquisition time (<5 min) is still less than the typical eukaryotic transcriptional time window ~30 min (21,22), soSPIM-FCS can access 3D dynamics within a biologically relevant timescale. Finally, we investigated the dynamics of Yes-associated protein (YAP) (23), a downstream effector of the Hippo signaling pathway. YAP is a transcriptional coactivator, whose nuclear localization is regulated by chemical and mechanical inputs (24). By imaging Dendra2-tagged YAP, our approach enabled us to estimate nuclear YAP diffusion kinetics for what we believe is the first time and demonstrate the dynamic heterogeneity of YAP in the nucleus. By measuring YAP dynamics throughout a large area of the cell nucleus, we expect our results to be unbiased due to localized variations in YAP dynamics (e.g., due to association with DNA via TEAD-binding).

MATERIALS AND METHODS

Detailed description on imaging FCS, data fitting, microfabrication, and the protocol for cell culture can be found in the Supporting Material.

Experimental setup and data collection

The soSPIM system is composed of a high numerical aperture (NA) objective (CFI Plan Apochromat VC 60× WI 1.27 NA; Nikon Instruments, Melville, NY), a beam steering unit, and dedicated microfabricated devices containing mirrors angled at 45° alongside microwells (Fig. 1; Fig. S1 in the Supporting Material). The soSPIM components are mounted on a conventional inverted microscope (model No. Ti-E, with 1.5× lens of the microscope body and a 0.45× lens to ensure a pixel size of 160 nm in the image plane for sCMOS camera and 266 nm pixel size for EMCCD camera; Nikon Instruments). The microfabricated imaging chamber (Fig. S2 (19)) is placed on an axial translation piezo stage within a controlled environment chamber for live cell imaging. Fluorescence emission is collected through

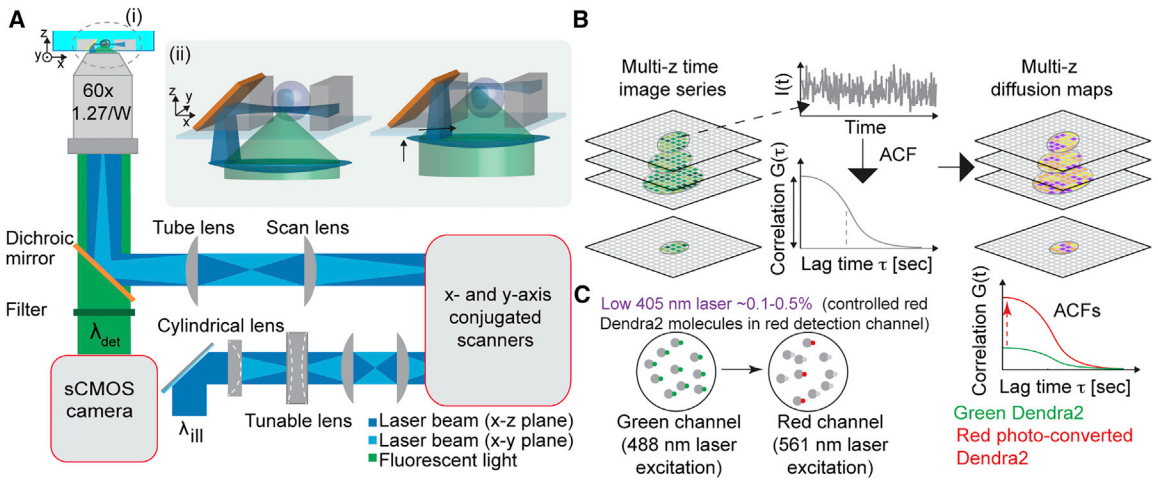

FIGURE 1 Experimental setup of single-objective based multiplexed-multiplane FCS (soSPIM-FCS) measurements. (*A*) (*i*) Experimental setup of the soSPIM system. (*ii*) Closeup of the 45° micromirror angled to reflect the light-sheet beam orthogonal to the detection axis for imaging at two different depths. (*B*) Principle of multiplane FCS measurements. In multiplane imaging FCS, a sequential time image series is acquired at different z position in a cell and the time autocorrelation performed at every pixel of the plane to achieve multiplane diffusion and concentration maps. (*C*) Principle of using photoconvertible protein for FCS. (*Left*) The number of the photoconverted red molecule can be tuned in the observation volume by 405 nm laser excitation. (*Right*) Dendra2 protein in red form is expected to show increased ACF amplitude. To see this figure in color, go online.

the same objective used for excitation and is captured in streaming mode on a sCMOS camera. The whole acquisition process is steered using MetaMorph software (Molecular Devices, Sunnyvale, CA).

The tunable lens and the galvanometric mirrors (Fig. 1 *A*) were precisely aligned and conjugated to the objective back focal plane to ensure the light sheet to be perpendicular to the microscope objective optical axis after reflection onto the 45° mirror, regardless of its reflection position. Drifting of the light sheet along the x axis when performing 3D imaging is compensated by calibrating the light-sheet position at two different depths. Further details of soSPIM setup are described in Galland et al. (19). A cylindrical lens (f = 150 mm; Thorlabs, Newton, MA) may be inserted thanks to a switchable mount into the optical path to focalize the laser beam in one direction at the objective back focal plane. It enables us to create a static light sheet in the sample for FCS acquisition. The cylindrical lens is mounted on a rotational mount to align its focalization direction with the 45° mirror's long axis.

Imaging FCS characterization and calibration for soSPIM

The thickness of the excitation light-sheet was characterized by imaging 100 nm tetraspeck beads embedded in 1% agarose gel filling the microwells (1:100 ratio; Fig. S3). The light-sheet characteristics can subsequently be extracted from $\omega(x) = \omega_o\sqrt{1 + ((x - x_0)/Z_R)^2}$, where ω_0 is the beam waist, representing half the minimum thickness e_0 of the light-sheet; Z_R is the Rayleigh length, corresponding to half the size of the field of view of the light-sheet; and x_0 is the position of the beam focalization along the propagation direction. For a 3 mm diameter excitation beam at the cylindrical lens position, we measured $e_0 = 1.8 \pm 0.2$ μm and $Z_R = 13 \pm 0.5$ μm at 561 nm wavelength (Fig. S3).

The width of the static light sheet created by inserting a cylindrical lens into the beam steering optical path (f = 150 mm) was characterized by imaging the light-sheet through a fluorescent polymer after reflection on the mirror (Fig. S3 *B*). Fitting the width of the light-sheet by a Gaussian function, we estimate the width of the light-sheet to be 26 ± 1 μm (full width half-maximum).

The laser power density was then calculated as the power spread over an area of 18 × 26 μm^2, which corresponds to the XY area of the light-sheet.

Imaging FCS data acquisition

For imaging, the growth media was replaced by 2 mL of imaging media composed of FluoroBrite media (Gibco/Thermo Fisher Scientific, Waltham, MA) supplemented with 10% FBS and 10 mM of HEPES buffer in a 35 mm dish, to ensure minimal fluorescence background.

For FCS imaging, a region of interest (ROI) of between 32 × 32 and 100 × 60 pixels was chosen, centered on the sample inside the camera field of view. Time series of 10–20 k frames per plane were acquired at 2.4–4.3 ms integration time for live cell imaging, and time series in the range 50–100 k frames per planes were acquired at 155 μs integration times for beads and single fluorophore imaging. The objective axial position stability was ensured by the Perfect Focus System of the microscope body (Nikon Instruments). For live cell FCS imaging, up to eight time-series at different z positions (dz = 0.8 μm) were acquired. For FCS imaging of U2OS Dendra2-Pol II cells and MKN28 Dendra2-YAP cells, acquisitions were performed by excitation with the 561 nm laser (laser power in between 0.5 and 1.5 kW/cm^2). The 405 laser power (0.05–0.2 kW/cm^2) was adjusted to continuously photoconvert a sparse subset of Dendra2 proteins, ensuring sufficient SNR for FCS analysis while renewing photobleached fluorophores to allow up to eight planes to be acquired on a single cell. Tables S1 and S2 summarize the different camera settings, data acquisition, and postprocessing parameters used in the article.

All imaging FCS data were corrected for fluorescence bleaching, with detailed description of the data fitting, typical defects, and photobleaching correction available here in Krieger et al. (8), and the analysis was performed using QFit3.0 and/or ImageJ imaging FCS plugin (25,26).

RESULTS

soSPIM-FCS characterization and validation

We calculated ACFs using fluorescent beads and organic dyes. To minimize variation due to self-aggregation of beads, buffer pH was kept at ~10 (use M/10 NaOH solution to adjust pH) and the beads were sonicated before use, while Atto 565 dye was first dissolved in DMSO and further diluted in 1 × PBS buffer at pH7.4. Fig. 2 *A* shows typical ACFs for 100 nm fluorescent beads (*red*) and Atto 565 organic dyes (*gray*) in buffer solution, with dashed lines representing fits to Eq. S2 (see the Supporting Material; see also Fig. S4). By varying the effective camera pixel size (by postprocessing) we estimated the lateral extension of the point spread function (PSF)—the value at which the predicted diffusion coefficient is independent of pixel size—to be 0.7 μm (Fig. 2 *B*). The bead and Atto565 dye average diffusion coefficients were $D_{22°C} = 4.8 \pm 1.8$ μm^2/s and 220 ± 40 μm^2/s, respectively, at room temperature, although note this likely underestimates diffusivity for organic dyes due to slow camera exposure (27). The bead diffusion data were in good agreement with single point confocal measurements (see Fig. S4 and Table S3; setup as described in Maharana et al. (28)). Furthermore, the corresponding cumulative distribution function (CDF) for the fitted diffusion coefficients at room temperature (Fig. 2 *C*) were in a similar range to previously reported SPIM-FCS measurements (8,20). Finally, in principle, a freely diffusing particle should have a linear relationship between the effective area (determined here by the camera pixel size and binning) and the diffusion time, with zero intercept (29,30). By plotting the change of diffusion time (y axis) with the change in effective area (x axis, postprocess binning; Fig. 2 *D*), we see that the relationship is close to linear, with $D_{22°C} \sim 3.3 \pm 1.3$ μm^2/s at room temperature, in good agreement with the fitting to the ACFs from Eq. S2 (see the Supporting Material). These calibration and FCS sensitivity tests (8) show that the presented soSPIM-FCS setup can be reliably used for FCS measurements (see comparison with other methods in Table S3).

To further test the FCS capabilities of soSPIM, we next performed sequential multiplane soSPIM-FCS to live NIH3T3 cells expressing stable eGFP-tagged H2B histone. Cells were prepared as described in the Supporting Material. The reflected light-sheet was positioned on the cell nucleus and multiple z planes were sequentially illuminated. For each section a time image series of 20 k frames was collected at 2.4 ms camera exposure on an EMCCD camera (using a cropped field of view). The time image series were autocorrelated (see Eq. S1) at each pixel and fitted with a one-diffusive component model, Eq. S2 (see also the

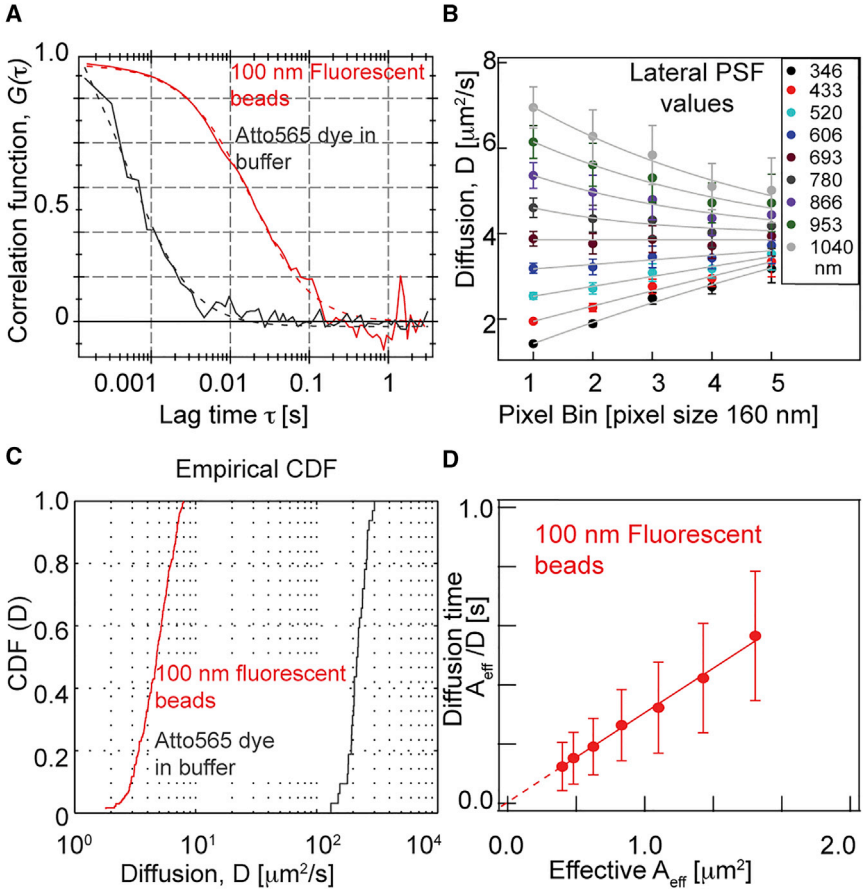

FIGURE 2 Imaging FCS calibration and sensitivity of soSPIM-FCS. (*A*) Typical single pixel autocorrelation function for 100 nm tetra-spec fluorescent beads (*red*) and organic Atto565 dye (*gray*) in 1 × PBS buffer. Data were acquired with a sCMOS camera using a 32 × 32 (32 × 16 organic dyes) pixel ROI at 155 μs camera integration time. (*Dashed lines*) Fits of Eq. S1; see the Supporting Material. (*B*) Dependence of diffusion coefficient, *D*, at different camera pixel binning and lateral PSF (analysis was performed with varying binning values from 1 × 1 to 5 × 5 pixels). (*C*) The diffusion coefficient cumulative distribution function for 100 nm fluorescent beads and Atto 565 dyes in 1 × PBS. (*D*) Dependence of the diffusion time on the effective area (postacquisition camera binning). Inverse slope estimates the diffusion coefficient ($D_{22°C} = 3.3 \pm 1.3$ μm²/s for 100 nm fluorescent beads). Experiments were performed on a sCMOS camera with a pixel size of 160 nm. ACF analysis were performed with varying binning values from 1 × 1 to 5 × 5 pixels. To see this figure in color, go online.

Supporting Material) (8). Fig. S5, *A* and *B* (for two different cells), shows the diffusion coefficient maps and distribution at two different planes, with an average diffusion value 0.28 ± 0.08 μm²/s (average 2300 pixels). To test sensitivity, we measured the effect of DNA-binding drug Hoechst 33342 (which induces cell death) on histone diffusion in the same cell. After treatment, the average fluorescence signal showed higher intensity and the diffusion coefficient decreased to 0.16 ± 0.06 μm²/s (Fig. S5 *C*). The decreased diffusion coefficient may be due to shrinkage of the whole chromosome structure as the nucleus shrinks during apoptosis (31). The diffusion CDF was markedly changed after Hoechst drug treatment (Fig. S5 *D*), showing that soSPIM-FCS is sensitive to dynamic changes inside the nucleus.

The important result of this analysis is that the slow histone protein diffusion, particularly after Hoechst 33342 treatment, showed fast fluorescence bleaching. High-quality FCS measurements could thus not be achieved for more than three consecutive planes. Due to the high expression and low mobility of many nuclear localized proteins it is technically challenging to obtain good estimates of diffusion coefficients without significant photobleaching in live cells. To tackle these challenges, photoconvertible fluorophores are needed to control the number of active molecules in the focal volume to achieve high-quality FCS measurements across the whole nucleus.

Improved multiplex FCS using photoconvertible fluorophore Dendra2

FCS in living cells requires an optimal number of particles in the observation volume: too few and the signal is significantly affected by the detector background; too many and the ACFs are too flat and noisy. Controlling the protein expression of fluorescently tagged proteins is often difficult in practice. To overcome this challenge, prebleaching before FCS was previously used to reduce the effective number of fluorescent protein molecules in live cells (32,33); however, this may induce severe photodamage and precludes multiplane imaging due to rapid loss of total fluorescence signal in a living sample. An alternative way to overcome protein overexpression without bleaching is to use photoactivatable fluorescent proteins (5,10). The density of fluorescent proteins can be easily tuned by adjusting the intensity of the 405 nm laser, allowing a high SNR ratio for FCS, as demonstrated recently in the early mammalian embryo (5,10).

To test the sensitivity of photoconvertible tagged proteins for camera-based imaging FCS in live cells, we used stably expressing Dendra2-Pol II U2OS cells (34). Dendra2 was converted from green to red fluorescence using a 405 nm excitation laser (34–36), with the number of photoconverted molecules controlled by varying the 405 nm laser excitation power. Fig. 3 shows the characterization of eGFP- and Dendra2-tagged proteins for FCS in live cells. The fluorescence signal from the photoconverted red form of Dendra2 showed long-term stability (>3 min) compared to eGFP-tagged proteins (Fig. 3 *A*). Most importantly, the ACFs were significantly improved with Dendra2 compared to eGFP (Fig. 3, *B* and *C*), with lower noise and subsequently improved data fitting.

We compared the ACFs of the different Dendra2 emissions on confocal-based single-point FCS. The ACF amplitude (inversely proportional to concentration, Eq. S2; and see the Supporting Material) was significantly increased in photoconverted (*red*) Dendra2 expressing cells compared with the green channel (Fig. 3, *D* and *E*). Further, we confirmed using Dendra2-NLS (to avoid binding kinetics) that varying the activation of Dendra2 alters the observed particle number, but not the measured diffusion time, Figs. 3 *F* and S6. Hence, photoconversion allows precise control of the number of active fluorescent molecules for FCS analysis and this significantly improves the quality of fitting to the measured ACFs.

Sequential, multiplane imaging FCS

We now combined soSPIM-FCS with Dendra2 to obtain sequential multiplane, multiplexed FCS. We imaged stable Dendra2-Pol II U2OS cells using soSPIM-FCS, with a total of eight planes per cell with z spacing = 0.8 μm. A stable 561 nm laser power of $\approx$0.8 kW/cm^2 was used with a stable low 405 nm activation dose (~0.05 kW/cm^2). The bottom and top planes of a serum-stimulated U2OS cell nucleus are shown in Fig. 4, *A* and *B*, respectively, along with their (unnormalized) ACFs (*right side*). Although there is a decrease in quality at the top plane (primarily due to photobleaching), the ACF was still of sufficient quality for reliable model fitting. The diffusion maps for all eight planes of a serum-stimulated cell are shown in Fig. 4 *C* (see Fig. S7 for further examples). The diffusion coefficient of RNA Pol II typically ranged from 1 to 5 μm^2/s, which is similar to other transcription factors in the cell nucleus (3,37). Fig. 4 *D* shows orthogonal views of the diffusion maps along x, y, and z axes. Structures are apparent in the diffusion maps; these are consistent with different chromosomal packing at different nuclear positions (2) (see also Movies S1 and S2).

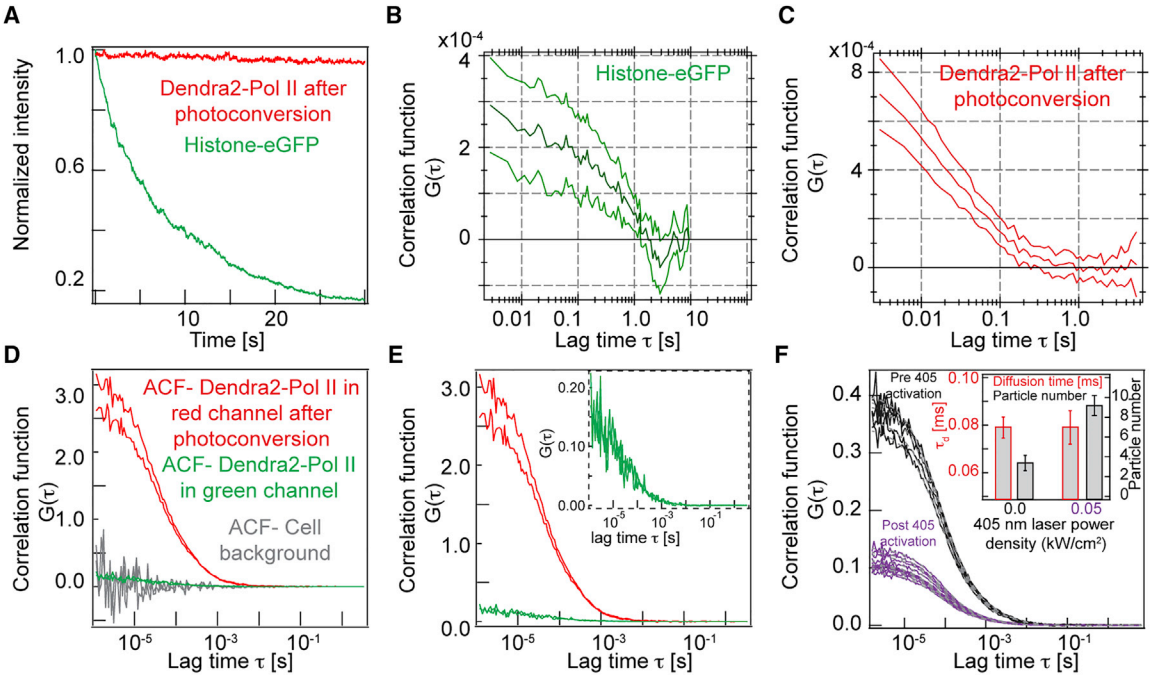

FIGURE 3 Characterization of Dendra2 fluorescent protein for FCS imaging. (*A*) Typical intensity profiles for eGFP and red photoconverted Dendra2 protein in imaging FCS. (*B* and *C*) Average autocorrelation functions of eGFP (*B*) and Dendra2 (*C*). Upper and lower lines represent maximum extent of ACFs ($n = 36$). (*D*) ACFs, including cell background (*gray*), for Dendra2 protein (*green*), and photoconverted in the red channel with point FCS on a confocal FCS setup. (*E*) As for (*D*), but without background and the inset shows a magnified view of the ACF in the green channel. (*F*) Change in ACF amplitude for Dendra2-3xNLS under different 405-nm laser activation. (*Inset*) There is no change in diffusion time, but the particle number increases after photoconversion of Dendra2 green to red fluorophore in the red channel detection. Histone-eGFP experiments were performed on an EMCCD camera with effective pixel size = 266 nm and Dendra2-Pol II on a sCMOS sensor with effective pixel 160 nm. To see this figure in color, go online.

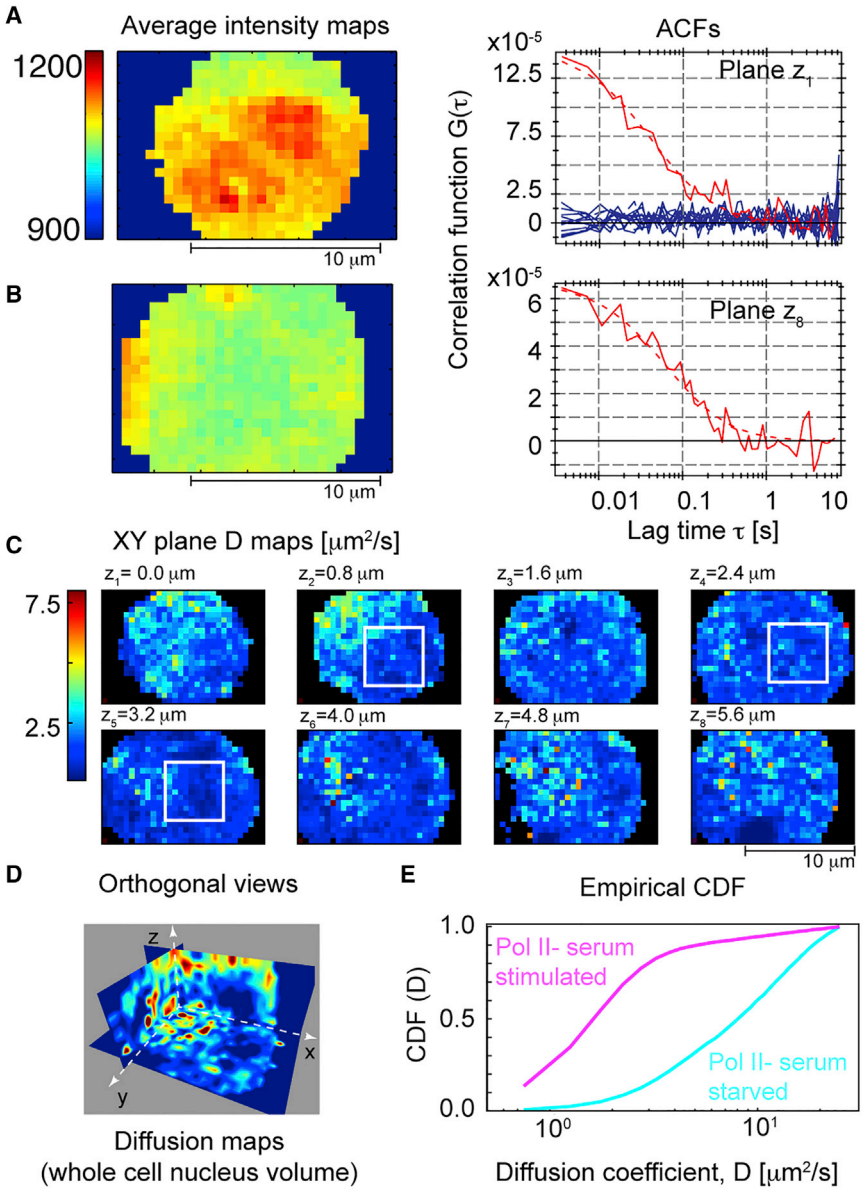

FIGURE 4 Multiplane, multiplexed diffusion maps of Dendra2-Pol II expressed in U2OS cells. (*A* and *B*) Average intensity maps of Dentra2-Pol II time image series (*left*) and corresponding ACFs (*right*). 10 k images were acquired at different z positions (*A*, $z_+ = 0.0$ μm; *B*, $z_8 = 5.6$ μm) with a spacing of ~0.8 μm and all eight planes were sequentially imaged with a total time of 5 min. The regions outside the cell nucleus showed zero correlation (flat ACFs in *A* shown in *blue*). (*C*) Representative diffusion maps for Dendra2-Pol II in the cell nucleus at different z positions (see Movie S2). (*D*) 3D orthogonal view of diffusion maps along x, y, and z axes. (*E*) Cumulative probability distribution of diffusion coefficient in serum-starved (*cyan*) and stimulated (*magenta*) environments (average from four cells; >13,400 data points for serum-stimulated and >4800 data points for serum-starved conditions). All imaging performed on a sCMOS camera with effective pixel size = 160 nm. ACF analysis was performed with 3 × 3 pixel binning. To see this figure in color, go online.

To validate our analyses, we repeated the experiments on serum-starved cells (cells were starved at least 18 h before imaging), and diffusion values were compared between serum-stimulated and -starved conditions. In serum-starved cells, smaller Pol II clusters are predicted due to a lower transcriptional activity, hence an increase in the diffusion coefficient is expected. This was confirmed by comparison of the diffusion coefficient CDF for the two conditions (Fig. 4 *E*). Taken together, these results suggest that our approach is sensitive to spatial variations in Pol II dynamics. Although previous work has performed single molecule tracking of Pol II localization, this is inherently limited in number and spatial range. Here, we can describe the global (on the scale of the nucleus) Pol II dynamics in an unbiased manner. Qualitatively, we observe that diffusion appears slowest toward the cell center (Figs. 4 *C* and S7)—where chromosomes are more densely packed (38,39)—although a more comprehensive analysis is needed to confirm this. Therefore, our approach here provides an effective tool for exploring nuclear protein dynamics.

Recent observations in live cells suggest that Pol II clusters are dynamic and transient in nature during serum stimulation (34,40,41). Consistent with this, we observe distinct regions of slow dynamics in the diffusivity maps (Fig. 4 *D*). To explore this further, we performed a more careful analysis of the interplane variation in the diffusion maps. Fig. 5, *A* and *B*, shows representative cross-sectional diffusion map views along the *xz*- and *yz* planes. The diffusion coefficient maps measured for each plane (~36 s acquisition per plane) demonstrate spatial correlation in the z direction

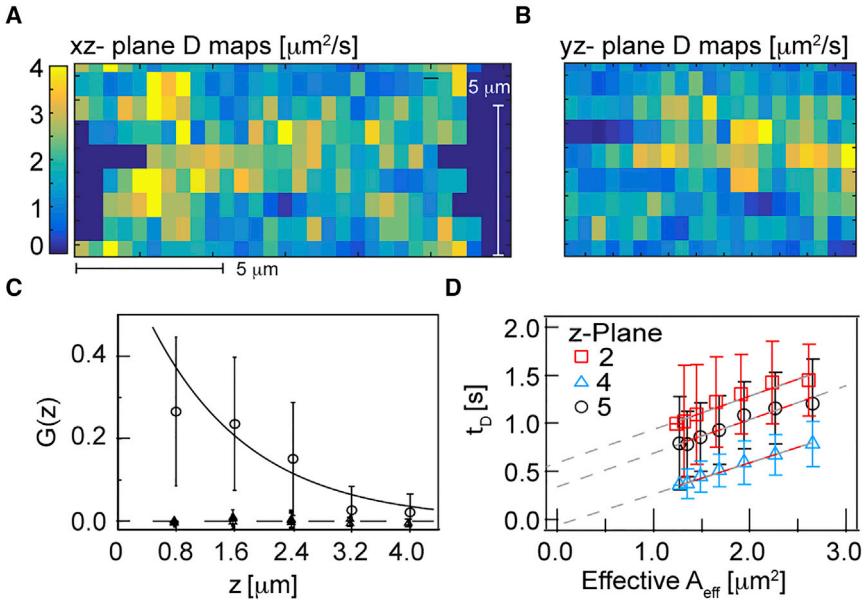

FIGURE 5 Spatial analysis of Dendra2-Pol II sequential multiplane, multiplexed diffusion maps. (*A* and *B*) Cross-section diffusion map views along *xz*- and *yz* planes (pixel size: 0.48 × 0.8 μm). (*C*) Spatial Pearson correlation coefficient along *z* direction ($n = 4$ cells), where the line is fit to $se^{-z/\lambda}$: $s = 0.75$ and $\lambda = 1.7$ (with 95% confidence interval [0.5, 3.0]). (*D*) Representative diffusion law plots for Dendra2-Pol II in serum-stimulated condition shows varying *y* axis intercepts (ROI for diffusion law analysis is shown by *white rectangle* for planes 2, 4, and 5 in Fig. 4 *C*). Experimental FCS details as in Fig. 4. To see this figure in color, go online.

over a distance of 1.7 μm (~3 planes along *z* direction) (Fig. 5 *C*). This diffusion correlation length is unlikely an artifact of the microscope setup, as planes are taken sequentially and hence correlations between planes in the diffusivity are most likely due to conserved Pol II dynamical structures, and not due to overlap of the PSF—we see correlations in diffusivity between planes imaged over a minute apart. Also, this naïve vertical diffusion correlation is likely an underestimate of structure extent, as most structures will not lie vertically in the *z* axis of the microscope. To test this further, we applied the FCS diffusion laws (as in Fig. 2 *D* (29,30,42)). Serum-stimulated cells in different *z* planes showed positive and varying *y* axis intercepts (Fig. 5 *D*; Fig. S8). A positive *y* intercept suggests possible spatially confined domains. Similar organization of Pol II and other nuclear proteins has been previously observed from single particle imaging and tracking (34,36). Alternatively, spatially varying diffusivity might be from local changes in effective viscosity due to chromosome organization, and these regions can effect transcriptional activity (43). The dynamic heterogeneities we measure may arise from local spatial heterogeneities in transcription activity, evolving on timescales >1 min.

Dendra2-YAP dynamics

We next extended our analysis to investigate the dynamics of YAP, a transcriptional coactivator. It is known that shuttling of YAP between the cytoplasm and nucleus is important for YAPs function in regulating the Hippo pathway. Thus we anticipate that YAP will be present in both the cytoplasm and nucleus, and we expect that YAP will exhibit reduced and heterogeneous diffusion dynamics in the nucleus as it can associate with DNA-binding transcription factors to regulate numerous downstream target genes.

MKN28 cells stably expressing Dendra2-YAP were generated (see the Supporting Material) and imaged with the soSPIM-FCS setup using a stable 561 nm laser power (≈0.5–0.8 kW/cm^2), and a low 405 nm activation dose to continuously activate a sparse subset of the Dendra2 protein. Time-series of 10 k frames were acquired at 4.3 ms integration time on 90 × 60 pixels ROI every 0.8 μm on up to seven planes in a single cell, which covers a significant portion of the nuclear volume.

Fig. 6 *A* shows the diffusion maps (akin to Fig. 4 *C*) for Dendra2-YAP, with corresponding intensity maps shown in Fig. S9 *A* (see Fig. S9 for other representative cells as well). Heterogeneity of YAP diffusion is apparent, with some spatial structure preserved between planes. This structure may indicate possible binding events between YAP and its targets within spatially conserved regions. The measured ACFs were well fitted by diffusion-dominated dynamics (Fig. S7 *B*); however, due to the temporal resolution of the cameras, we are principally identifying the dynamics of the slow (bound) fraction. To estimate the effective mean YAP diffusivity, we averaged all intranuclear ACFs and found $D_{YAP} \sim 4.5 \pm 2.2$ μm^2 s^{-1} (compared with D_{YAP} ~4.2 ± 2.0 μm^2 s^{-1} using eGFP-YAP in the cell nucleus on confocal FCS; Fig. S10). Despite having a large standard deviation, the diffusion probability functions for different planes are comparable (Fig. 6 *C*), suggesting that this is a reliable estimate of YAP diffusivity. Because nuclear-localized YAP associates with DNA-binding proteins, YAP diffusion in the nucleus was slower compared to cytoplasmic diffusion (note, to capture the faster cytoplasmic dynamics—$D_{YAP,CYT}$ ~80 μm^2 s^{-1}—we used confocal FCS; Fig. S10). Because we measure the diffusivity across nearly the entire nucleus, our

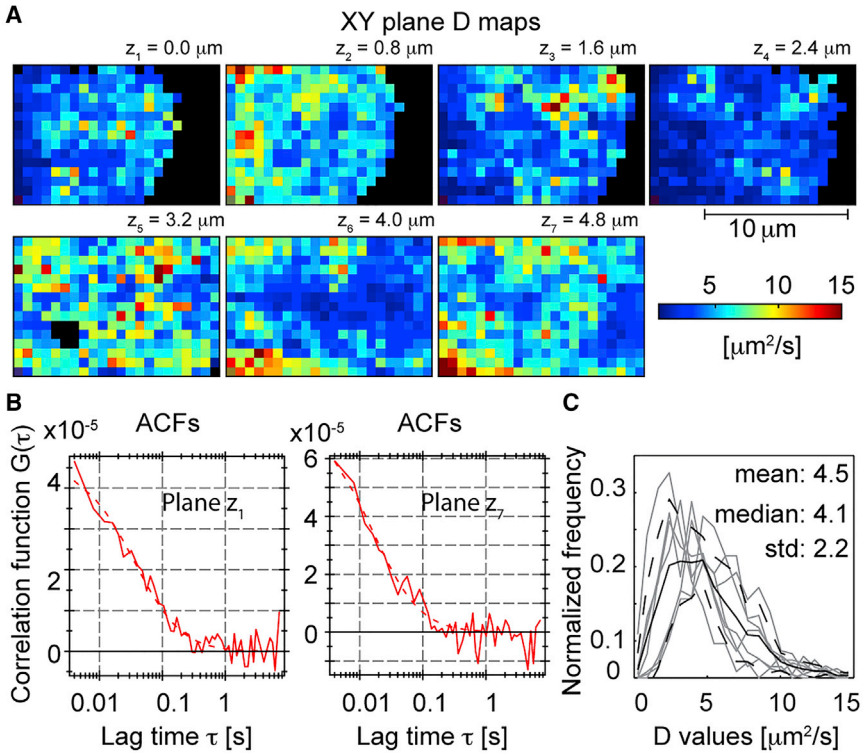

FIGURE 6 Multiplane diffusion maps of Dendra2-YAP protein in cell nucleus. (*A*) Dendra2-YAP diffusion maps (similar to Fig. 4 *C*) at different planes in the cell nucleus (*z* spacing 0.8 μm). See Fig. S9 for mean intensity images. (*B*) Representative ACF of Dendra2-YAP in the cell nucleus (fit in *dashed line*). (*C*) Diffusion coefficient probability distribution (*solid black line*) of Dendra2-YAP for all seven planes (*dashed lines* represent ± 1 SD). (*Gray*) Distributions for individual planes. All images were performed on a sCMOS camera with effective pixel size = 160 nm. ACF analysis was performed with 4×4 pixel binning. To see this figure in color, go online.

results represent a good estimate of the overall effective YAP nucleus diffusion. To our knowledge, the data presented here is the first quantitative measurement of YAP dynamics within the cell nucleus. With further improvements in detector sensitivity, we anticipate being able to dissect spatial variation in nuclear YAP dynamics in the future as we can access faster timescales in a spatially extended manner. An interesting future direction would be to explore the fraction of freely available YAP simultaneously in the cytoplasm and nucleus (including transport into the nucleus), and how this responds to external stimuli such as mechanical stress (44,45). This may give important insight into the dynamics of YAP as a transcriptional coactivator and how the cell responds rapidly to external stress.

DISCUSSION

Heterogeneity of protein dynamics are often the signature of local changes in protein activity. Developing techniques that enable mapping of such spatial heterogeneity could provide key inputs into our understanding of protein function. soSPIM-FCS provides a 3D mapping of the dynamics of cellular processes. The unique soSPIM-FCS architecture reported here provides distinct improvements on previous multiplex FCS methods: 1) high sectioning capability at the single cell level; 2) high mechanical stability as compared to the standard two-objective SPIM setup; 3) the possibility to use high numerical aperture objectives for efficient signal collection ensuring sensitivity at the single molecule level (19); and 4) the ability to combine localized activation (and other quantitative techniques such as fluorescence recovery after photobleaching, FRAP) using the inverted microscope with the soSPIM sensitivity and low photobleaching and phototoxicity. The power to combine photoconversion of fluorophores with FCS in a spatially extended manner is perhaps the strongest element of this approach. Further, all the functionality of a standard inverted microscope (differential interference contrast, phase, epifluorescence, etc.) can be readily used to position and select the sample. This provides clear practical advantages over the classical SPIM approaches.

Data presented here demonstrates that the soSPIM configuration is stable and sensitive enough to produce high quality ACFs. Coupling the SPIM configuration with photoconvertible fluorophores allowed us to sufficiently reduce protein photobleaching so that we can measure up to eight diffusion maps spaced by 0.8 μm. This approach provided a more precise 3D reconstruction of the nuclear dynamic environment. We validated the efficacy of our setup with two quite different proteins in the nucleus. We established that Dendra2-Pol II has a nonhomogeneous distribution of diffusivity at different spatial positions within the nucleus, consistent with single molecule tracking approaches (34). However, our approach encompasses orders-of-magnitude more measurements per cell. We demonstrated the power of our approach by providing an estimate

of the effective nuclear diffusion of the transcriptional coactivator YAP. Such an estimate is not significantly affected by local structures in the nucleus due to the large number of data points collected for each cell. Of course, camera-based FCS still has limitations, particularly in terms of the relatively slow frame rates (milliseconds here versus microseconds on confocal-based FCS) and bleaching effects for longer imaging time windows. We have carefully assessed that photophysics effects from using a photoconvertible fluorophore do not distort our conclusions. The results presented here represent a significant improvement over most previous camera-based FCS studies and we have validated results using confocal FCS.

Being able to measure dynamics in three dimensions is an important step to link the existence of local dynamical heterogeneities to biological structures. Indeed, local fluctuation of diffusion coefficients may transiently arise in the cell or may be due to intrinsic noise of the detection system. However, the existence of correlated regions of diffusion coefficient heterogeneities at different z positions for Pol II strongly suggests that the observed dynamical variations arise from differential local interactions of proteins. In future, we anticipate that the combination of soSPIM-FCS and photoconvertible proteins may become a powerful quantitative bioimaging tool to create differential diffusion and interaction maps of transcription factors and other proteins in vivo. Such information may be important, for example, in deciphering the role of transcription factor binding to determine cell fate (5), or understanding the role of spatio-temporal changes in the effective viscosity within the nucleus due to chromosomal reorganization and its effect on the rate of transcriptional kinetics (3). Single-particle tracking can also be achieved with this technique (46). Finally, the laser driving unit to implement the soSPIM is essentially a modified FRAP head. Our approach could thus readily combine FCS, single-particle tracking, and FRAP on the same system to probe a spectrum of protein dynamics ranging from millisecond to minutes.

SUPPORTING MATERIAL

Supporting Materials and Methods, ten figures, four tables, and two movies are available at http://www.biophysj.org/biophysj/supplemental/S0006-3495(16)34265-5.

AUTHOR CONTRIBUTIONS

A.P.S., and R.G. contributed equally to this work; A.P.S., R.G., V.V., and T.E.S. designed the project; A.P.S. and R.G. performed experiments and collected the raw data and analyzed the FCS data; M.L.F.-E. cloned the 3xNLS-Dendra2, Dendra2-YAP, and eGFP-YAP constructs, and generated the stably expressing cell lines; G.G. designed and implemented the microwells; R.G., J.-B.S., V.S., and V.V. designed and built soSPIM and adapted it for performing FCS; A.P.S., R.G., V.V., and T.E.S. wrote the article; and all authors participated in discussion and editing of the article.

ACKNOWLEDGMENTS

Authors thank Prof. Shivashankar for stable H2B-eGFP NIH3T3 cells, Prof. Xavier Darzacq for stable Dendra2- Pol II U2OS cells, and the Electronic Imaging Center of the Bordeaux Imaging Center for the metallization of the devices. The authors acknowledge the Michael W. Davidson group, The Florida State University, Tallahassee, FL for provision of all Dendra2 and eGFP cDNAs.

A.P.S. was supported under a National Research Foundation (NRF) Fellowship awarded to T.E.S. (grant No. 2012NRF-NRFF001-094). This work was also supported by the Ministère de l'Enseignement Supérieur et de la Recherche (ANR soSPIM, Labex BRAIN and ANR-10-INBS-04 France-BioImaging), the Centre National de la Recherche Scientifique and the Conseil Régional d'Aquitaine.

REFERENCES

1. Woringer, M., X. Darzacq, and I. Izeddin. 2014. Geometry of the nucleus: a perspective on gene expression regulation. *Curr. Opin. Chem. Biol.* 20:112–119.
2. Makhija, E., D. S. Jokhun, and G. V. Shivashankar. 2016. Nuclear deformability and telomere dynamics are regulated by cell geometric constraints. *Proc. Natl. Acad. Sci. USA.* 113:E32–E40.
3. Hager, G. L., J. G. McNally, and T. Misteli. 2009. Transcription dynamics. *Mol. Cell.* 35:741–753.
4. Macháň, R., and T. Wohland. 2014. Recent applications of fluorescence correlation spectroscopy in live systems. *FEBS Lett.* 588:3571–3584.
5. White, M. D., J. F. Angiolini, …, N. Plachta. 2016. Long-lived binding of Sox2 to DNA predicts cell fate in the four-cell mouse embryo. *Cell.* 165:75–87.
6. Capoulade, J., M. Wachsmuth, …, M. Knop. 2011. Quantitative fluorescence imaging of protein diffusion and interaction in living cells. *Nat. Biotechnol.* 29:835–839.
7. Singh, A. P., and T. Wohland. 2014. Applications of imaging fluorescence correlation spectroscopy. *Curr. Opin. Chem. Biol.* 20:29–35.
8. Krieger, J. W., A. P. Singh, …, T. Wohland. 2015. Imaging fluorescence (cross-) correlation spectroscopy in live cells and organisms. *Nat. Protoc.* 10:1948–1974.
9. Struntz, P., and M. Weiss. 2016. Multiplexed measurement of protein diffusion in *Caenorhabditis elegans* embryos with SPIM-FCS. *J. Phys. D Appl. Phys.* 49:044002.
10. Kaur, G., M. W. Costa, …, N. Plachta. 2013. Probing transcription factor diffusion dynamics in the living mammalian embryo with photoactivatable fluorescence correlation spectroscopy. *Nat. Commun.* 4:1637.
11. Hebert, B., S. Costantino, and P. W. Wiseman. 2005. Spatiotemporal image correlation spectroscopy (STICS) theory, verification, and application to protein velocity mapping in living CHO cells. *Biophys. J.* 88:3601–3614.
12. Wiseman, P. W. 2013. Chapter Ten—Image correlation spectroscopy: mapping correlations in space, time, and reciprocal space. *In* Methods in Enzymology. Y. T. Sergey, editor. Academic Press, New York, pp. 245–267.
13. Hedde, P. N., M. Stakic, and E. Gratton. 2014. Rapid measurement of molecular transport and interaction inside living cells using single plane illumination. *Sci. Rep.* 4:7048.
14. Krieger, J. W., A. P. Singh, …, J. Langowski. 2014. Dual-color fluorescence cross-correlation spectroscopy on a single plane illumination microscope (SPIM-FCCS). *Opt. Express.* 22:2358–2375.
15. Szaloki, N., J. W. Krieger, …, G. Vamosi. 2015. Evidence for homodimerization of the c-Fos transcription factor in live cells revealed by fluorescence microscopy and computer modeling. *Mol. Cell. Biol.* 35:3785–3798.

16. Mohan, K., S. B. Purnapatra, and P. P. Mondal. 2014. Three dimensional fluorescence imaging using multiple light-sheet microscopy. *PLoS One.* 9:e96551.

17. Abrahamsson, S., J. Chen, …, M. G. L. Gustafsson. 2013. Fast multicolor 3D imaging using aberration-corrected multifocus microscopy. *Nat. Methods.* 10:60–63.

18. Prevedel, R., Y.-G. Yoon, …, A. Vaziri. 2014. Simultaneous whole-animal 3D imaging of neuronal activity using light-field microscopy. *Nat. Methods.* 11:727–730.

19. Galland, R., G. Grenci, …, J. B. Sibarita. 2015. 3D high- and super-resolution imaging using single-objective SPIM. *Nat. Methods.* 12:641–644.

20. Singh, A. P., J. W. Krieger, …, T. Wohland. 2013. The performance of 2D array detectors for light sheet based fluorescence correlation spectroscopy. *Opt. Express.* 21:8652–8668.

21. Ben-Ari, Y., Y. Brody, …, Y. Shav-Tal. 2010. The life of an mRNA in space and time. *J. Cell Sci.* 123:1761–1774.

22. Molina, N., D. M. Suter, …, F. Naef. 2013. Stimulus-induced modulation of transcriptional bursting in a single mammalian gene. *Proc. Natl. Acad. Sci. USA.* 110:20563–20568.

23. Sudol, M. 1994. Yes-associated protein (YAP65) is a proline-rich phosphoprotein that binds to the SH3 domain of the Yes proto-oncogene product. *Oncogene.* 9:2145–2152.

24. Yu, F. X., B. Zhao, and K. L. Guan. 2015. Hippo pathway in organ size control, tissue homeostasis, and cancer. *Cell.* 163:811–828.

25. Wohland, T. 2015. imFCS Plugin for ImageJ. National University of Singapore http://www.dbs.nus.edu.sg/lab/BFL/imfcs_image_j_plugin.html.

26. Krieger, J. W., and J. Langowski. 2015. QuickFit 3.0 (GPL 3.0). https://github.com/jkriege2/QuickFit3.

27. Sankaran, J., N. Bag, …, T. Wohland. 2013. Accuracy and precision in camera-based fluorescence correlation spectroscopy measurements. *Anal. Chem.* 85:3948–3954.

28. Maharana, S., D. Sharma, …, G. V. Shivashankar. 2012. Dynamic organization of transcription compartments is dependent on functional nuclear architecture. *Biophys. J.* 103:851–859.

29. Bag, N., S. Huang, and T. Wohland. 2015. Plasma membrane organization of epidermal growth factor receptor in resting and ligand-bound states. *Biophys. J.* 109:1925–1936.

30. Wawrezinieck, L., H. Rigneault, …, P.-F. Lenne. 2005. Fluorescence correlation spectroscopy diffusion laws to probe the submicron cell membrane organization. *Biophys. J.* 89:4029–4042.

31. Yu, S.-W., H. Wang, …, V. L. Dawson. 2002. Mediation of poly(ADP-ribose) polymerase-1-dependent cell death by apoptosis-inducing factor. *Science.* 297:259–263.

32. Kim, S. A., K. G. Heinze, and P. Schwille. 2007. Fluorescence correlation spectroscopy in living cells. *Nat. Methods.* 4:963–973.

33. Altan-Bonnet, N., and G. Altan-Bonnet. 2009. Fluorescence correlation spectroscopy in living cells: a practical approach. *Curr. Protoc. Cell Biol.* 4:24.

34. Cisse, I. I., I. Izeddin, …, X. Darzacq. 2013. Real-time dynamics of RNA polymerase II clustering in live human cells. *Science.* 341:664–667.

35. Buchholz, J., J. W. Krieger, …, J. Langowski. 2012. FPGA implementation of a 32x32 autocorrelator array for analysis of fast image series. *Opt. Express.* 20:17767–17782.

36. Izeddin, I., V. Récamier, …, X. Darzacq. 2014. Single-molecule tracking in live cells reveals distinct target-search strategies of transcription factors in the nucleus. *eLife.* 3:e02230.

37. Gorski, S. A., M. Dundr, and T. Misteli. 2006. The road much traveled: trafficking in the cell nucleus. *Curr. Opin. Cell Biol.* 18:284–290.

38. Cremer, T., and C. Cremer. 2001. Chromosome territories, nuclear architecture and gene regulation in mammalian cells. *Nat. Rev. Genet.* 2:292–301.

39. Horn, P. J., and C. L. Peterson. 2002. Molecular biology. Chromatin higher order folding—wrapping up transcription. *Science.* 297:1824–1827.

40. Zhao, Z. W., R. Roy, …, X. S. Xie. 2014. Spatial organization of RNA polymerase II inside a mammalian cell nucleus revealed by reflected light-sheet superresolution microscopy. *Proc. Natl. Acad. Sci. USA.* 111:681–686.

41. Chen, X., M. Wei, …, Y. Sun. 2016. Study of RNA Polymerase II clustering inside live-cell nuclei using Bayesian nanoscopy. *ACS Nano.* 10:2447–2454.

42. Ng, X. W., C. Teh, …, T. Wohland. 2016. The secreted signaling protein Wnt3 is associated with membrane domains in vivo: a SPIM-FCS study. *Biophys. J.* 111:418–429.

43. Grünwald, D., R. M. Martin, …, M. C. Cardoso. 2008. Probing intranuclear environments at the single-molecule level. *Biophys. J.* 94:2847–2858.

44. Halder, G., S. Dupont, and S. Piccolo. 2012. Transduction of mechanical and cytoskeletal cues by YAP and TAZ. *Nat. Rev. Mol. Cell Biol.* 13:591–600.

45. Santinon, G., A. Pocaterra, and S. Dupont. 2016. Control of YAP/TAZ activity by metabolic and nutrient-sensing pathways. *Trends Cell Biol.* 26:289–299.

46. Chen, J., Z. Zhang, …, Z. Liu. 2014. Single-molecule dynamics of enhanceosome assembly in embryonic stem cells. *Cell.* 156:1274–1285.

Biophysical Journal, Volume *112*

Supplemental Information

3D Protein Dynamics in the Cell Nucleus

Anand P. Singh, Rémi Galland, Megan L. Finch-Edmondson, Gianluca Grenci, Jean-Baptiste Sibarita, Vincent Studer, Virgile Viasnoff, and Timothy E. Saunders

Probing dynamic architecture of nuclear proteins in 3D with photo-convertible imaging fluorescence correlation spectroscopy

Anand P. Singh[1,†], Rémi Galland[2,3,†], Megan L. Finch-Edmondson[1,4], Gianluca Grenci[1], Jean-Baptiste Sibarita[2,3], Vincent Studer[2,3], Virgile Viasnoff[1,5,6]*, and Timothy E. Saunders[1,5,7]*

[1]Mechanobiology Institute, National University of Singapore, Singapore

[2]Institut Interdisciplinaire de Neurosciences, University of Bordeaux, France

[3]CNRS UMR 5297, University of Bordeaux, France

[4]Department of Physiology, National University of Singapore, Singapore

[5]Department of Biological Sciences, National University of Singapore, Singapore

[6]CNRS UMI 3639, Singapore

[7]Institute for Molecular and Cell Biology, A*Star, Singapore

[†]These authors contributed equally to this work.

*Co-corresponding authors Virgile.Viasnoff@espci.fr and dbsste@nus.edu.sg

Supplementary Material

Materials and methods

Imaging FCS and data fitting

Imaging FCS analyzes the variation in the time-dependent intensity autocorrelation function (ACF). In imaging FCS, each pixel of the 2D array detectors camera yields fluorescence intensity fluctuations from a small observation volume, over a period of typically ~20-40 sec at high framerate of up to 250-1000 fps. Temporal intensity fluctuations can be used to infer the underlying dynamics (or photo-physical fluorescence fluctuations) of the fluorescently-tagged molecules. The ACF for a fluorescent signal collected over time is given by $G(\tau)$

$$G(\tau) = \frac{\langle \delta I(t) \cdot \delta I(t+\tau) \rangle}{\langle I(t) \rangle^2} + G_\infty , \qquad (1)$$

where $G(\tau)$ is the normalized autocorrelation function, τ the correlation time, $I(t)$ represents the instantaneous fluorescence intensity at time t, $\delta I(t)$ the change in fluorescence intensity (deviation from mean value $\delta I(t) = I(t) - \langle I \rangle$), $\langle -- \rangle$ denotes time averaging, and G_∞ is the correlation at long time or the correlation offset value.

To infer dynamic parameters, we fit the measured ACF (Eq. 1) with the prediction from a molecule diffusing in three-dimensions $G_{3D}(\tau)$ (see detailed derivation elsewhere (1)):

$$G_{3D}(\tau) = \frac{1}{N\sqrt{1+\frac{4D\tau}{w_z^2}}} \left[\frac{\frac{\sqrt{4D\tau + w_{xy}^2}}{\sqrt{\pi}.a} \left\{ e^{-\frac{a^2}{4D\tau + w_{xy}^2}} - 1 \right\} + \operatorname{erf}\left(\frac{a}{\sqrt{4D\tau + w_{xy}^2}} \right)}{\operatorname{erf}\left(\frac{a}{w_{xy}} \right) + \frac{w_{xy}}{\sqrt{\pi}.a} \left\{ e^{-\left(\frac{a}{w_{xy}}\right)^2} - 1 \right\}} \right]^2 + G_\infty , \qquad (2)$$

The measurable parameters are the camera pixel size a in object space, the lateral, and axial PSF size w_{xy}, w_z,. The variables fitted are the diffusion coefficient D, the average particle N, and the correlation convergence value G_∞.

Microfabrication wells for creating light sheet and cell holder

Micro-mirroring surfaces were produced in silicon wafer by anisotropic etching in alkaline solution. Micro-wells of 40x40 μm^2 were then created by deep reactive ion etching process through openings in AZ9260 positive tone resist. The silicon wafer with 45° mirroring surfaces and micro-wells were then replicated in a UV-curable and index-matched polymer on clean #1.5H coverslips in a two-step process: (i) replication of the silicon master mold in PDMS; (ii) reproduction of the PDMS imprint on a coverslip by capillary filling and UV-curing of the UV-curable polymer. The plastic chips were then coated with a thin layer of gold by thermal evaporation in a vacuum chamber to make the 45° surfaces reflective. After metallization, a flat PDMS stamp was deposited on top of the mirror to allow filling the gap in between the mirror by a UV-curable polymer layer by capillary filling. Once the polymer cured, the PDMS stamp was removed, and the metal coating outside the mirror was removed

by wet etching. The coverslip was finally sealed in a bottom-free 35 mm plastic dish that allowed easy surface passivation with 0.1% Pluronic solution overnight and cell seeding and culturing. Further details are described in (2).

soSPIM light sheet scanning unit and bead scan PSF characterization

The soSPIM beam steering unit is composed of a cylindrical lens, a tunable lens and a pair of galvanometric mirror. x- and y-axis positioning of the light-sheet in soSPIM are controlled by the galvanometric mirrors conjugated by two relay lenses. Scanning the excitation beam along the mirror long axis (y-axis) creates the light-sheet, and displacing the light-sheet along the mirror short axis (x-axis) changes the light-sheet depth into the sample. As an alternative to scanning the excitation beam, a cylindrical lens can also be used to create a static light-sheet. The positioning of the light-sheet waist on the sample ROI is achieved using a tunable lens (TL) which defocalizes the excitation beam away from the mirror. The focal length of the tunable lens is maintained by a built-in feedback loop system and set to position the thinnest part of the light-sheet at the sample.

The micro-fabricated device containing the cells was placed on the microscope stage and a 60x WI high NA objective was used for imaging. The orientation of the light-sheet relative to the mirror orientation was adjusted by a cylindrical lens rotational mount. The long axis of the mirror for the axial displacement of the light-sheet was determined according to the mirror orientation in the objective field of view. For two different positions of the light-sheet on the mirror, the axial position of the objective was adjusted to superpose the objective focal plane and the light-sheet, and the appropriate defocus strength was adjusted according to the distance of the sample from the micro-mirror. A custom-written MetaMorph plugin ensures the synchronization between the light-sheet displacement along the mirror with the axial position of the objective and the defocus strength by linear regression between these two calibration points.
To estimate the depth of focus and thickness of the light-sheet, the light-sheet, superposed to the objective focal plane, was scanned along the axial direction and the beads imaged with a step-size of 100 nm in the z-axis. The bead images were projected using maximum intensity along the x-axis and the axial dimension measured by Gaussian fitting along the z direction for each bead. The axial dimension of each bead (full width at half maximum) was then recorded according to their position from the 45° mirror. To estimate the width of the static light-sheet created inserting a cylindrical lens into the beam steering unit optical path, the light-sheet was imaged through a fluorescent polymer after reflection on the 45° mirror. The light sheet profile was then extracted and fitted with a Gaussian function to estimate its width (see Fig. S3).

Dendra2-YAP and 3xNLS-Dendra2 stable cell lines

The coding sequences for 3xNLS-Dendra2 and untagged Dendra2 with the stop codon removed were PCR amplified before being cloned into the retroviral expression vector pBABE puro using BamHI and EcoRI restriction sites. The coding sequence for human YAP isoform 1-2α (3) was then C-terminally sub-cloned in-frame with Dendra2 using EcoRI and SalI restriction sites to generate Dendra2-YAP.

Subconfluent HEK293T cells were co-transfected with pBABE puro 3xNLS-Dendra2 or Dendra2-YAP together with the pCL10A-1 packaging construct using TransIT-293 Transfection Reagent according to the manufacturers specifications. After 48h, the viral supernatants were collected, filtered, and mixed with polybrene before being added to subconfluent YAP null MKN28 cells that had been previously generated using CRISPR-Cas9.

After 24h stably-transduced cells were selected using puromycin before cells were used for imaging experiments.

Cell culture and seeding in micro fabricated wells

Stably expressing H2B-eGFP NIH3T3 Dendra2-Pol II U2OS cells were cultured in high glucose Dulbecco's modified eagle media, supplemented with 10% fetal bovine serum, 1% GlutaMAX and 1% penicillin/streptomycin. Stably expressing 3xNLS-Dendra2 and Dendra2-YAP MKN28 cells were cultured in RPMI 1640 media supplemented with 10% fetal bovine serum and 1% penicillin/streptomycin. All cells were maintained in 5% CO_2 at 37°C. The day prior to seeding into 40x40 μm^2 micro-wells, cells were cultured in 35 mm plastic dishes to ensure they reached 70% confluence on the day of seeding. Before seeding, cells were gently washed twice with 1X PBS and trypsinized for 2 mins. After removing the trypsin, cells were immersed in 1 mL of growth media, and allowed to recover for 10 mins in the incubator.

For cell seeding into the micro-wells, around 0.5 million cells were deposited onto the micro-wells and placed in the incubator for 15 mins, allowing the cells to fill the micro-wells by gravity. The density of cells was adjusted to ensure efficient seeding of the wells with one cell in each well. Cells remaining outside wells were removed by rinsing twice with media, and the device was filled with 2 mL of growth media. This seeding step was repeated up to three times to ensure a filling ratio of 60-80% of wells. The cells were then allowed to recover for one to three hours in growth media in the incubator before imaging.

Supplementary Figures

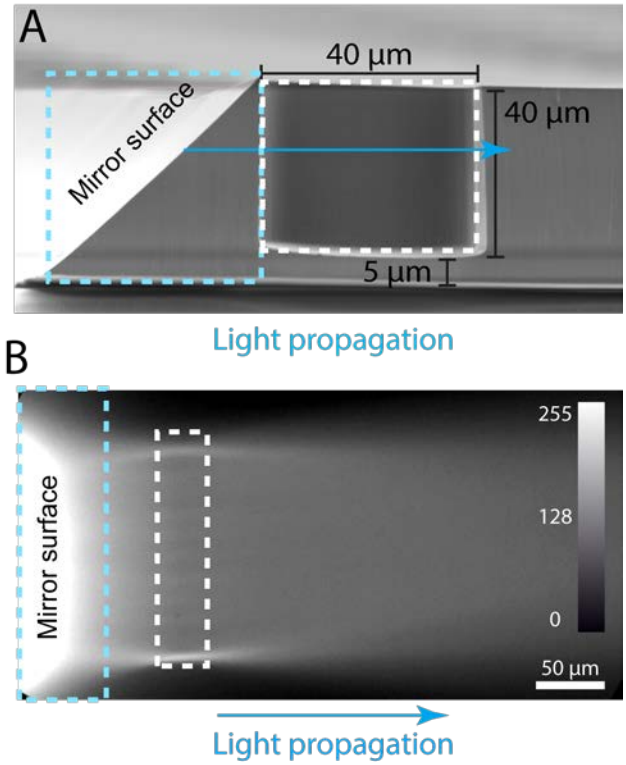

Figure S1: soSPIM light-sheet path. A: Sample mounting micro-well cross section view, the blue dotted region shows the mirror surface and white region shows the position of micro-well with respect to the mirror surface. B: Top view of the light-sheet after reflection on a 45° mirror and imaging through a fluorescent solution.

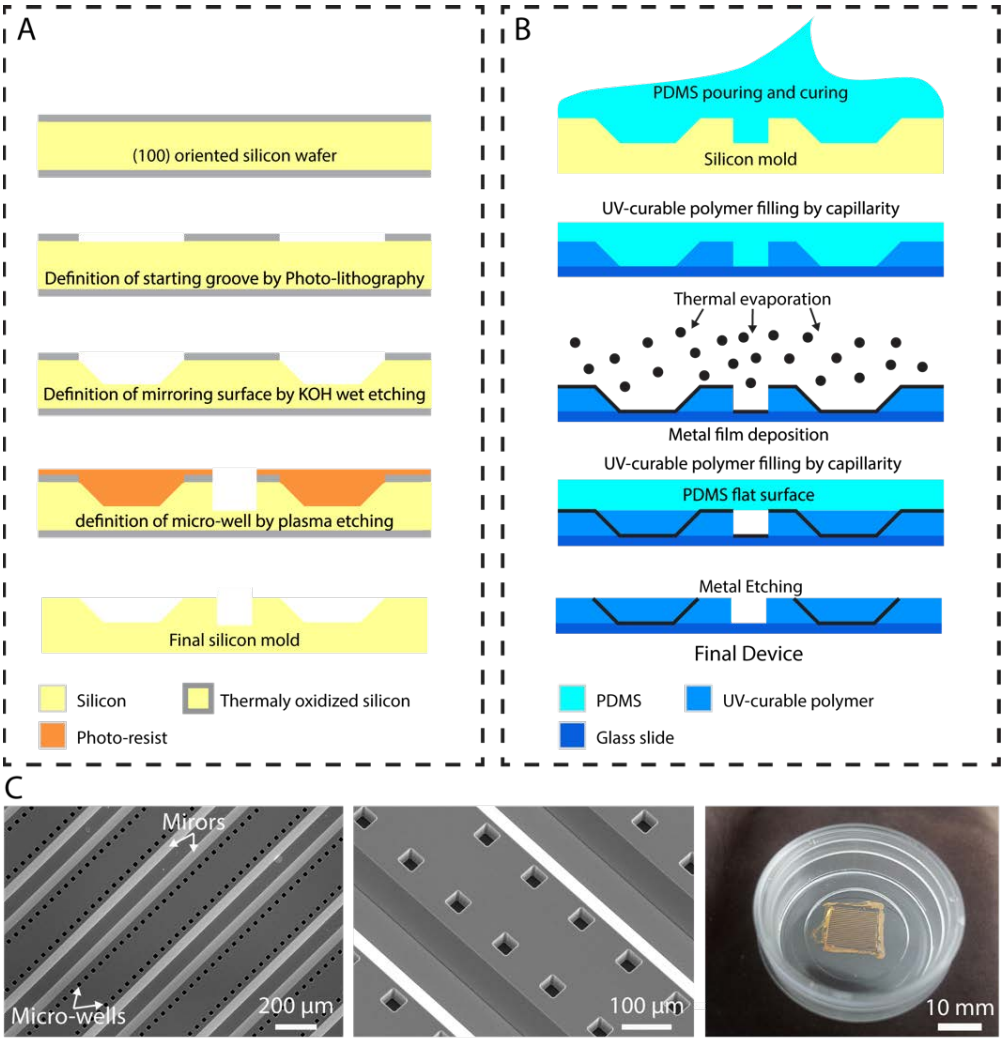

Figure S2: Micro-fabrication process of the device displaying 45° mirrors alongside micro-wells. A: Anisotropic wet etching and dry etching were sequentially used to create 45° surfaces and micro-wells respectively within a silicon wafer. B: Replication of the silicon wafer features onto coverslips and metallization of the 45° surfaces. A PDMS replica of the silicon wafer is created and then used to reproduce the wafer features onto a coverslip in a UV-curable polymer via a capillary filling process. The polymer surface is then coated with a metal layer to make the 45° surfaces reflective. Lastly, the 45° surfaces are protected by an additional layer of UV-curable polymer via a capillary filling process and the unprotected metal removed by wet etching. C: Left and middle panels: SEM images of a silicon wafer displaying 45° surfaces alongside micro-wells. Right panel: Image of a final device produced in a UV-curable polymer and metallized, and sealed on a bottom free plastic dish for easy cell culturing and handling.

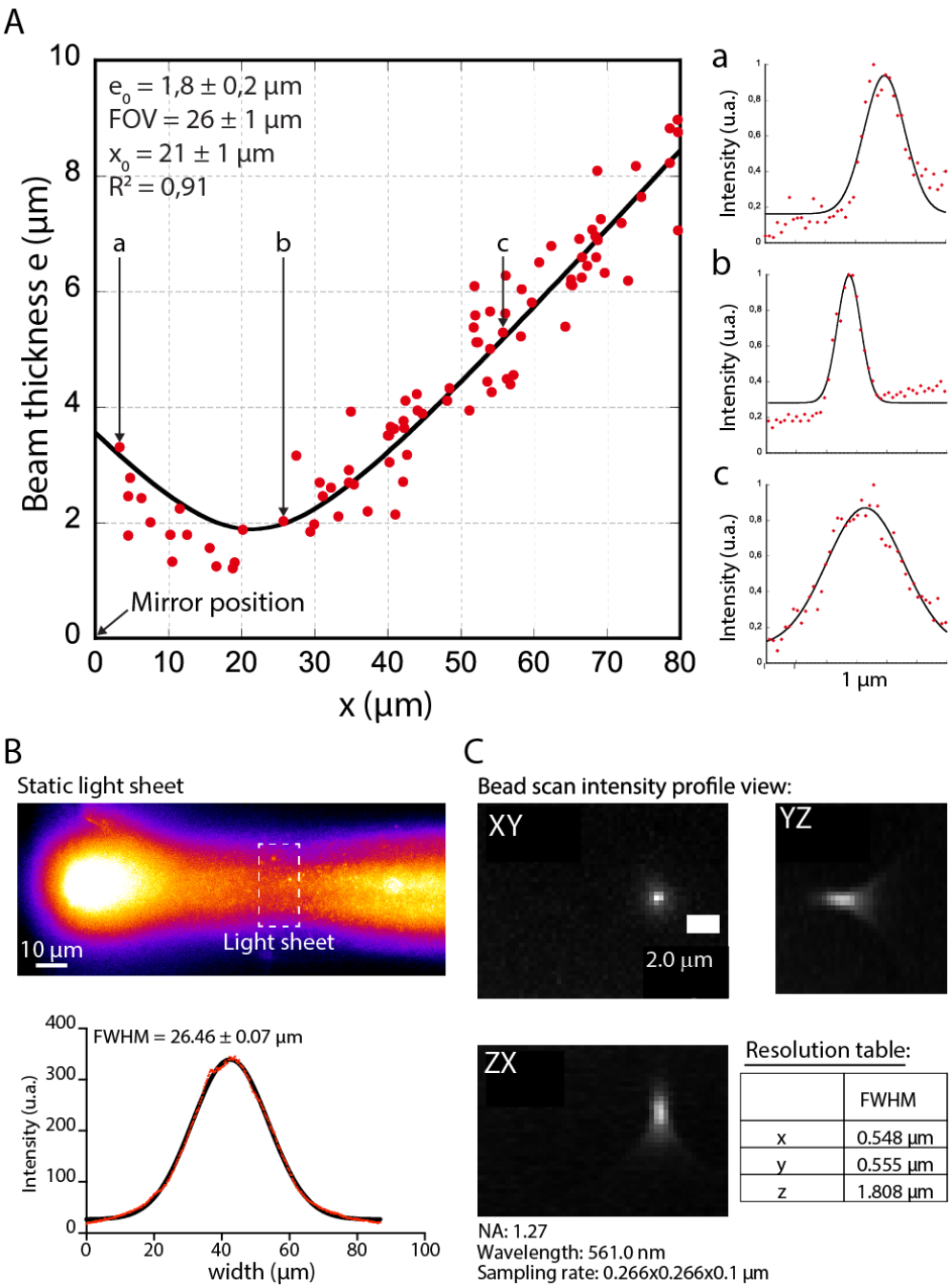

Figure S3: soSPIM light sheet profile characterization and PSF determination. A: Shows the axial dimensions (FWHM) estimated by Gaussian fitting of beads embedded in agar and imaged in the soSPIM configuration according to their position from the mirror (red dots). The black line represents the fit with the Gaussian beam propagation equation (see Methods in main text) and the reported value the result of the fit. The insets (a-c) represent the axial profile of three different beads (red dots) at different positions from the mirror (as highlighted in main panel) and their respective Gaussian fit (black line). B: Top-The light sheet imaged through fluorescent polymer after reflection on a 45° mirror (top Fig. S3). Bottom-

Protein dynamics within 3D cell nucleus

Experimental profile (red dots) and Gaussian fit (black line) of the light-sheet profile averaged on the whit box on top. The reported value is the fit result and represent the estimated static light-sheet width. C: PSF determined by bead scan. 100 nm fluorescent beads were embedded in 1% agarose and imaged on an EMCCD, Evolve512 (pixel size 266 nm), lateral (XY) and axial cross-sectional views (YZ, XZ) are shown. The line intensity was fitted with a Gaussian function and the typical values for lateral PSF are tabulated in the bottom right table.

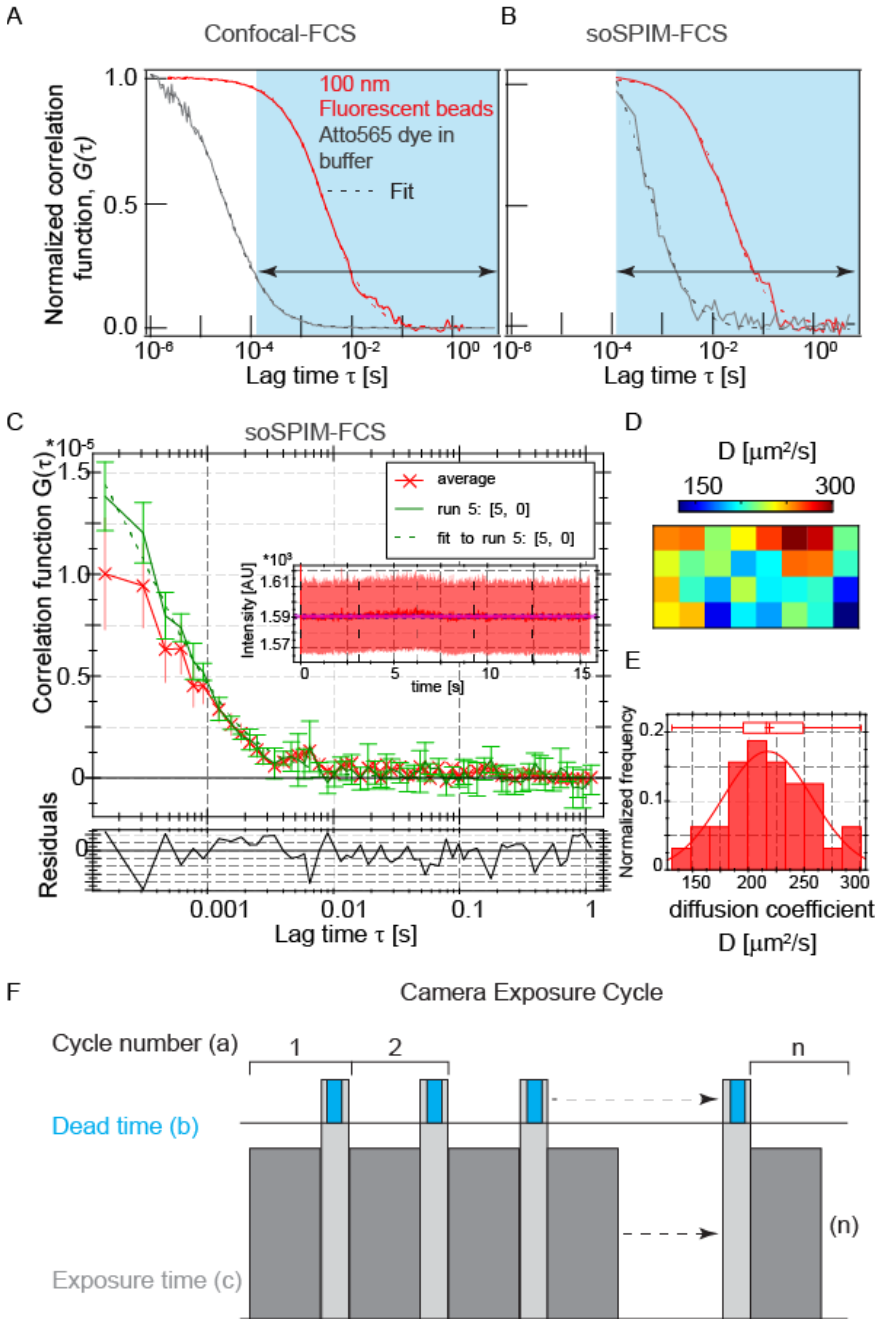

Figure S4: Typical autocorrelation function ACF obtained from Atto565 organic dyes (gray) and 100 nm fluorescent beads (red) in 1xPBS buffer. A-B: ACFs obtained on confocal FCS setup and on soSPIM-FCS setup respectively. Light blue region shows the time scale which can be captured on camera based FCS. Diffusion values obtained are tabulated in Table S3. Note: Due to slow acquisition rate (155 µs) of sCMOS camera diffusion coefficient of organic dyes will be underestimated than the actual value. In

addition, 100 nm fluorescent beads in buffer solution provides a good estimate of absolute diffusion coefficient (see Table S3). C: Autocorrelation function obtained from Atto565 organic dyes in 1xPBS buffer. Red curve shows the ACF from a single pixel and the average ACF for all the data points are shown in green. Inset image shows fluorescence intensity collected over time. D-E: Diffusion maps and histogram are shown. The average D value for Atto 565 dye for all the pixels is 220 ±40 $\mu m^2/s$. soSPIM data were acquired with an sCMOS camera using a 32x32 beads (32x16 organic dyes) pixel ROI at 155 μs camera integration time. Dashed lines correspond to fits of Eq. 2, see Supporting Material. F shows typical camera readout schemes. The pixel size for the analysis was 160 nm and the correlation analysis was performed with 4x4 pixel binning for dye and no binning for 100 nm fluorescent beads.

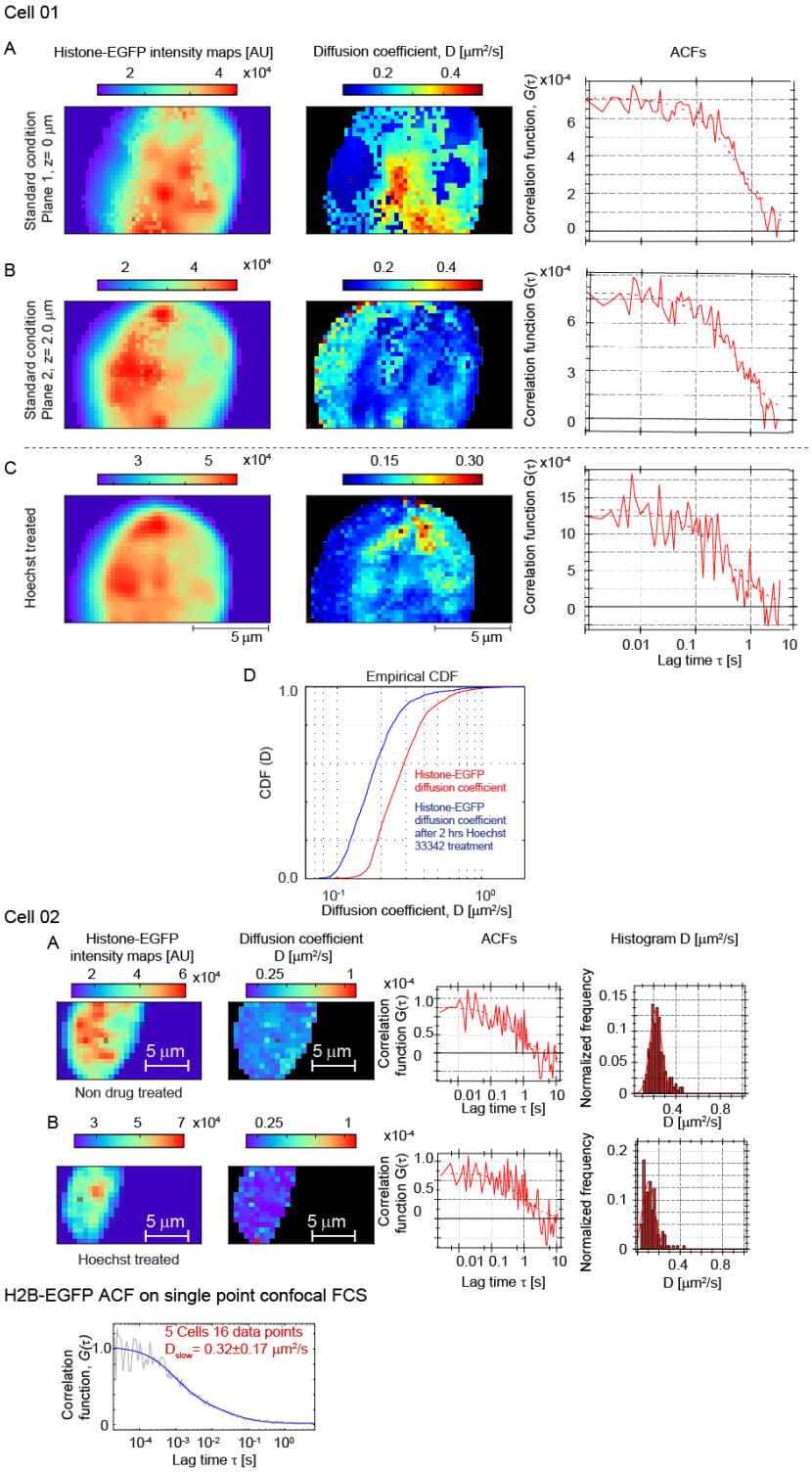

Figure S5: Multi-plane diffusion maps of H2B-eGFP protein in NIH3T3 cells collected on an EMCCD camera. Cell01:- A-B: FCS for two different

z-planes in the cell nucleus. Left - Average fluorescence intensity map for 20k frames; center - diffusion maps; right - typical ACFs. C: As (A) but after DNA binding drug treatment. D: Diffusion coefficient CDF before (red) and after (blue) DNA binding drug treatment. The pixel size for the analysis is 266 nm and the correlation analysis was performed without pixel binning. Cell02:- Similar treatment were performed on cell 2. Histone-EGFP diffusion before (A) and after (B) DNA-binding Hoechst 33342 treatment. Left: fluorescence intensity and diffusion maps. Right: ACFs and corresponding histogram of inferred diffusion coefficients. The pixel size for the analysis is 266 nm and the correlation analysis was performed with 2x2 pixel binning. Bottom figure shows the normalized ACF of Histone-eGFP in live cells at 37 °C on a single point confocal FCS setup.

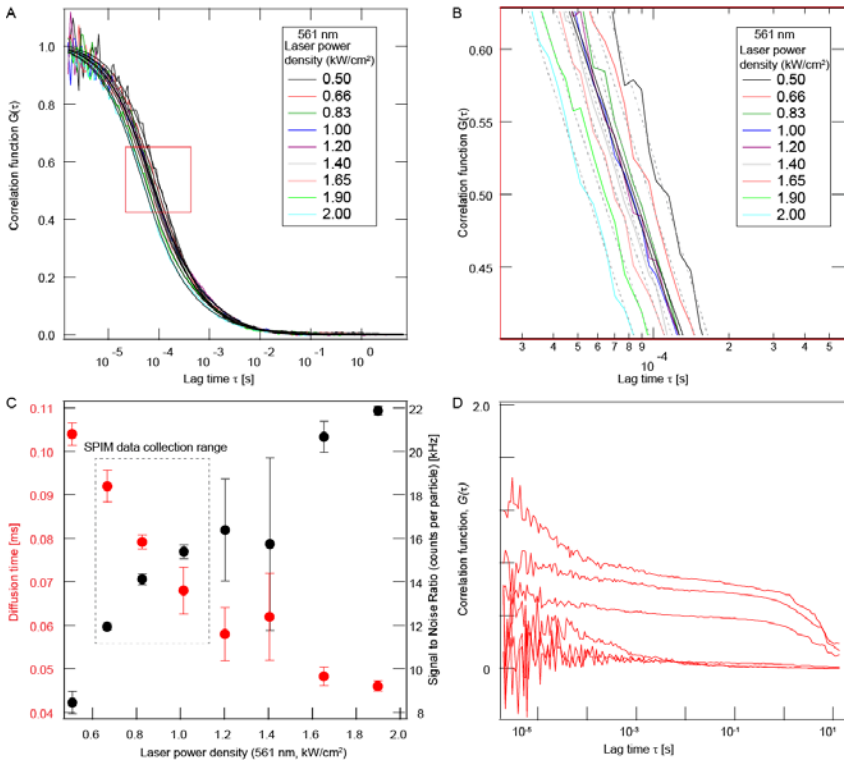

Figure S6: Characterization of 561 and 405 nm laser power dependence on diffusion time of Dendra2 protein. A: Shows ACFs of 3xNLS-Dendra2 ACFs at different 561 nm laser power (at constant 405 nm laser 0.05 kW/cm^2). B: Shows the zoomed red region of A. C: Shows continuous decrease in diffusion time (red left side) and increase counts per particle (black right side). D: Typical correlation function obtained from fixed cells expressing 3xNLS-*Dendra2* on a single point confocal setup.

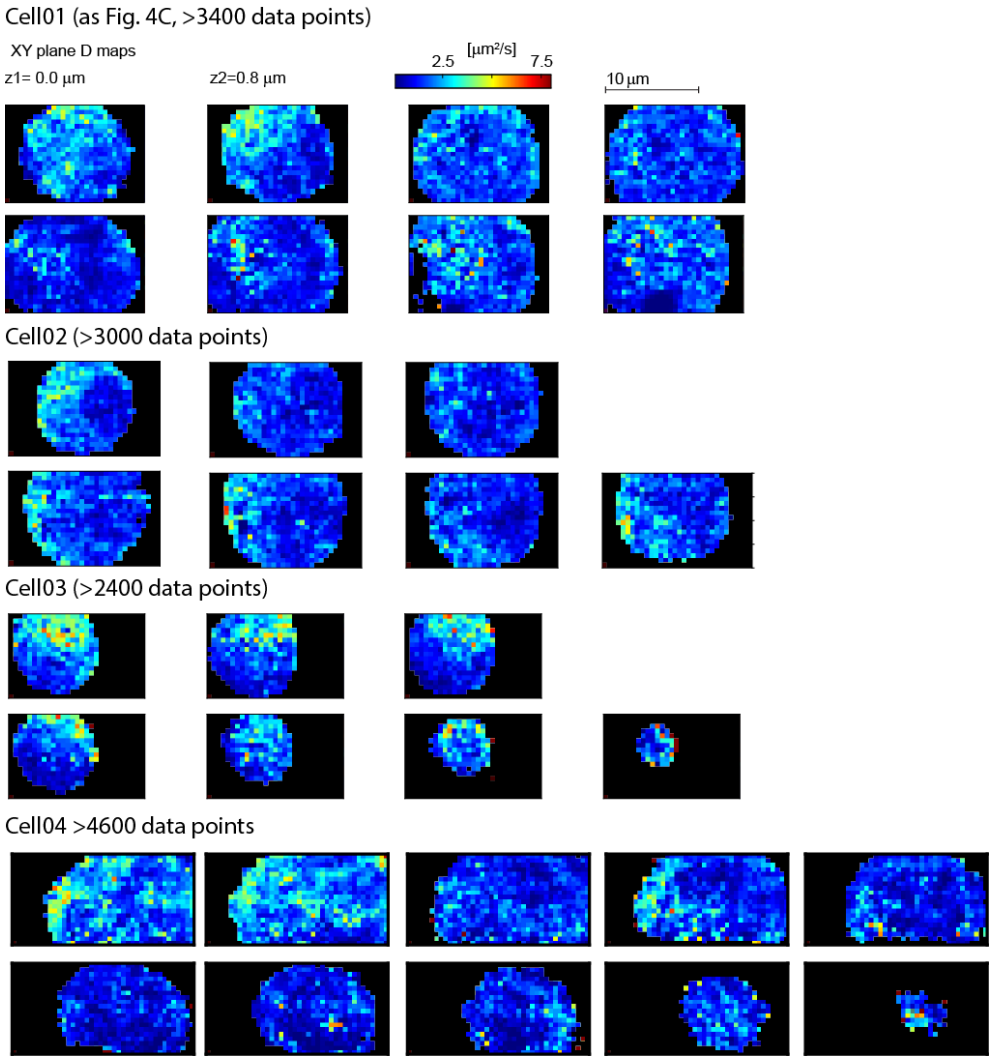

Figure S7: Representative diffusion maps for Dendra2-Pol II cell nucleus at different z-positions. All imaging performed on a sCMOS camera with effective pixel size = 160 nm. ACF analysis was performed with 3x3 pixel binning.

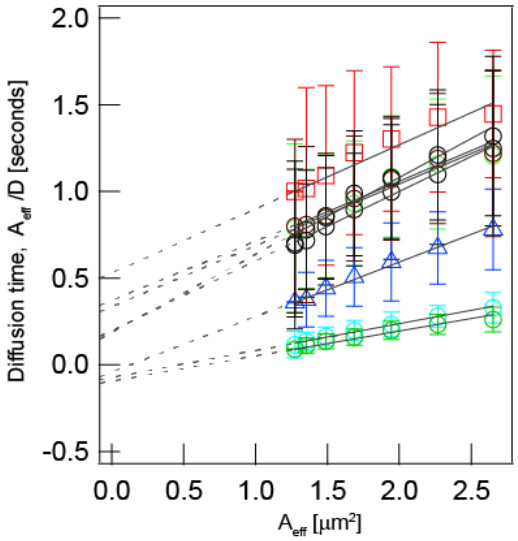

Figure S8: Representative diffusion law plots for Dendra2-Pol II in U2OS cell nucleus at different z-height. Similar to Fig. 5E but showing all planes.

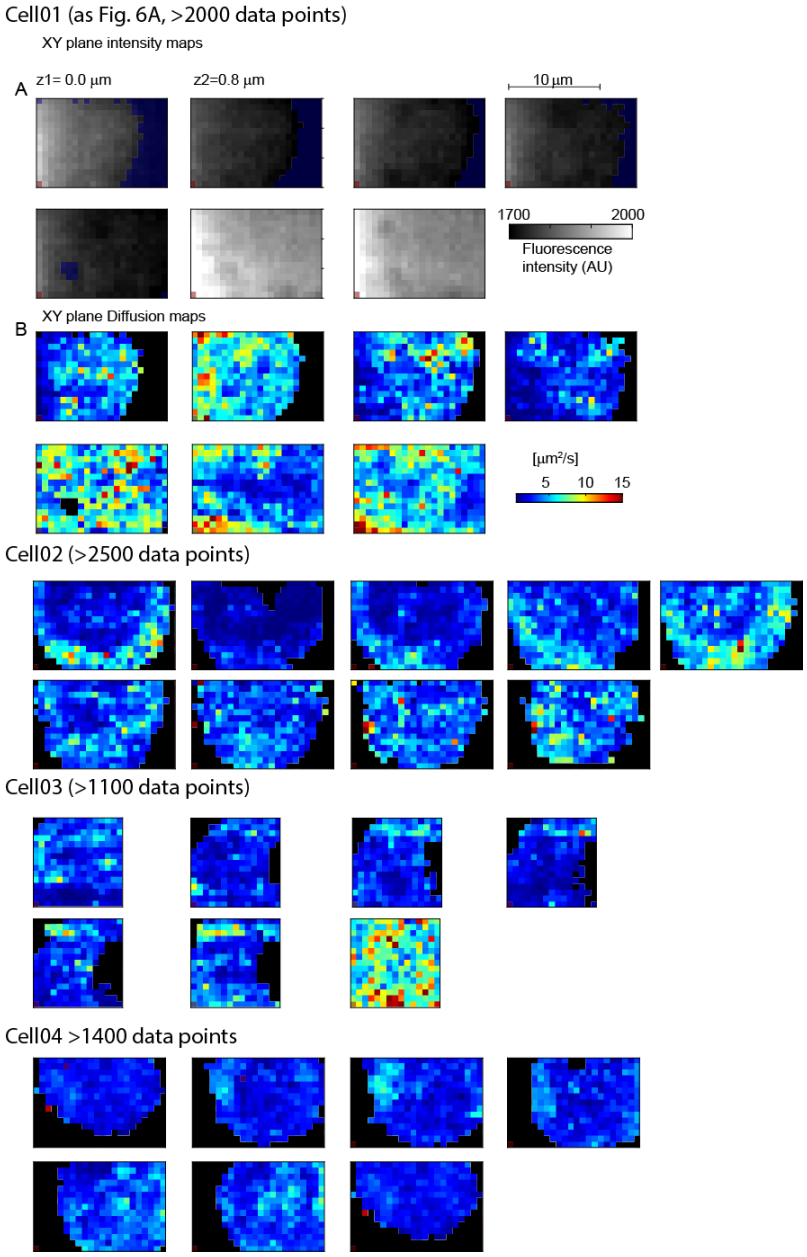

Figure S9: Representative diffusion maps for Dendra2-YAP cell nucleus at different z-positions. All imaging performed on a sCMOS camera with effective pixel size = 160 nm. ACF analysis was performed with 4x4 pixel binning.

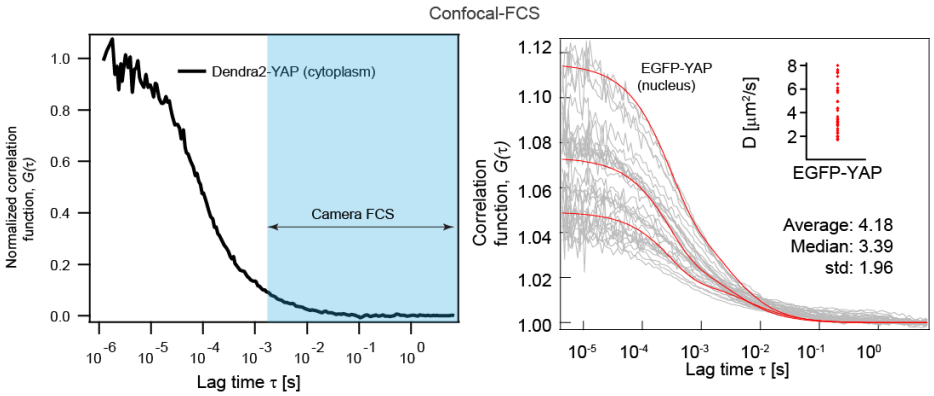

Figure S10: Left- Fast diffusion of Dendra2-YAP in cell cytoplasm performed on a confocal FCS setup at 37°C. Light blue region shows the time scale which can be captured on camera based FCS. Right- Auto-correlation functions obtained with eGFP-YAP on a single point confocal setup (gray curves show all measured profiles and the three red curves are representative fits). Inset: obtained diffusion coefficient value at 37 °C temperature with confocal FCS.

Supplementary Tables

Table S1 Typical camera exposure time and dead time for sCMOS and EMCCD sensors (see Fig. S4).

Type of sensor	Exposure time (ms)	Dead time (ms)
sCMOS Orca-Flash 2.0	0.0380	0.0015
EMCCD512 Evolve	2.00	0.38
EMCCD-iXon3 860 Andor	0.450	0.039

Table S2 Typical soSPIM-FCS data acquisition and post processing settings.

Camera settings	**EMCCD Evolve 512**	**sCMOS ORCA-Flash4.0**
Effective pixel size (μm)	16	6.5
Zoom factor	40-60x	40-60x
Pixel binning		
Data acquisition camera pixel bin	1	1
Postprocessing pixel binning		
• Bright samples (fluorescent beads in buffer)	1	1-3
• Organic dyes in buffer and fluorescent proteins	1-4	3-6
EM-gain	Yes	No EM gain
Bright fluorescent beads in buffer	10-100	NA
Organic dyes in buffer and fluorescent proteins	300	NA
Camera cycle time (ms)		
Organic dyes in buffer	--	0.016-0.160
Fluorescent beads in buffer	2-4	0.016-2.0
Fluorescent proteins in cells	2-5	2-5
Number of frames(k)/time(sec) required		
Organic dyes in buffer	--	60-120/20-40
Fluorescent beads in buffer	20-40/20-40	40-60/20-40
Fluorescent proteins	10-20/30-50	10-20/30-50
Laser Power	**kW/cm^2**	
405 nm laser (photoconversion to red)	0.05-0.2	
561 nm laser (FCS data acquisition)	0.5-1.5	

Table S3 Measured diffusion coefficient value of 100 nm fluorescent beads in 1xPBS (at pH=10) buffer and Histone protein in cell nucleus.

Sample @ °C	**D ($\mu m^2/s$)**	**Method used**	**Refs.**
100 nm Beads			
22 (lab temperature)	*4.80 ±1.80*	*soSPIM-FCS (1024 data points,*	
20 (scaled to 20°C)	*4.53 ±1.69*	*see* **Figure S4***)*	*This study*
25(scaled to 25°C	*5.20 ±1.94*	,,	
37 (scaled to 37°C)	*6.96 ±2.60*	,,	
22 (lab temperature)	*4.18 ±1.76*	,,	
		Confocal FCS (20 data points *see* **Figure S4***)*	
20	4.29	The theoretical diffusion coefficient (Stokes-Einstein relationship)	
20	3.80 ±1.00	SPIM-FCS	(4)
20	3.38 ±0.54	Coherent anti-stokes Raman scattering correlation spectroscopy	(5)
20	4.10 ±0.05	Single point confocal FCS	(4, 6)
21	4.13 ±1.16	3D tracking	(7)
25	4.4 ±0.70	Two focus FCS (2fFCS) and dynamic light scattering (DLS)	(8)
37	6.56 ±0.30	Temporal image correlation spectroscopy (TICS)	(9)
Fluorescent beads T7279	Invitrogen Singapore	100 nm TetraSpec beads	Fluorescent beads T7279
Histone protein in cell nucleus at 37°C			
H2B-EGFP	~0.28	soSPIM-FCS	This study
	~0.32	Confocal FCS	
HP1α-EGFP	0.16-0.4	camera based FCS	Supplementary Table S1. in (10)
Histone *Drosophila* His2Av::mRFP	~0.22	camera based FCS	Figure 9c in ref. (4)
H2A-GFP	~0.22	camera based FCS	See Table 1 in Ref. (4)
Dendra2-H2B	0.5	Single particle tracking	Figure 2—figure supplement 1 in (11)

Table S4 The list of microscope components and materials used in this manuscript.

SN	Name of the component and serial number	Company/ Supplier	Specifications and descriptions
1	Tunable lens Custom EL-30-10	Optotune	focal length from -80 mm to +1000 mm
2	Tube lens AC254-050-A	Thorlabs	focal length 50 mm
3	Galvanometric mirrors SCANMAX	Pangolin SCANMAX 506 actuators	with dielectric Chroma mirrors
4	Nikon Objective Plan Fluor 60x, 1.27 NA	Nikon	High NA objective
5	Telescope lens AC254-150-A	Thorlabs	tube lens of the microscope, focal length 150 mm for both lenses
6	Galvanometric control unit	Pangolin Laser Systems	Laser scanning unit
7	Microscope control software	MetaMorph software	Home written plugins in Visual basic NET
8	UV curable polymer OF-134	MyPolymer	Polymer
9	Pluronic solution F127	Sigma	Surface passivation
10	Fluorescent beads T7279	Invitrogen Singapore	100 nm TetraSpec beads
11	EMCCD 512	Evolve, Princeton Instruments	16 micron pixel size, QE 95 %
12	sCMOS ORCA-Flash4.0 V2	Hamamatsu Japan	6.5 micron pixel size, QE 70%
13	Atto 565 organic dye	Atto-Tech Germany	Carboxy AD 565-21
14	Hoechst 33342	Sigma Singapore	Concentration 0.2 μM for 35 mm culture dish.
15	HEPES buffer solution	Sigma Singapore	10 mM, pH range 6.8-8.2
16	Fetal Bovine Serum F2442	Sigma Singapore	Serum 10%
17	P0781 Penicillin-Streptomycin	Sigma Singapore	1% cell culture media

18	GlutaMAX	10567014 Invitrogen Singapore	1% Cell culture media
19	Agarose	A9414 Sigma Singapore	1.0 % agarose

References

1. Singh, A. P. 2014. Light sheet based fluorescence correlation and cross-correlation spectroscopy for quantitative measurements of bio-molecules in live cells. In Chemistry. National University of Singapore, Singapore.
2. Galland, R., G. Grenci, A. Aravind, V. Viasnoff, V. Studer, and J. B. Sibarita. 2015. 3D high- and super-resolution imaging using single-objective SPIM. Nat Meth 12:641-644.
3. Gaffney, C. J., T. Oka, V. Mazack, D. Hilman, U. Gat, T. Muramatsu, J. Inazawa, A. Golden, D. J. Carey, A. Farooq, G. Tromp, and M. Sudol. 2012. Identification, basic characterization and evolutionary analysis of differentially spliced mRNA isoforms of human YAP1 gene. Gene 509:215-222.
4. Krieger, J. W., A. P. Singh, N. Bag, C. S. Garbe, T. E. Saunders, J. Langowski, and T. Wohland. 2015. Imaging fluorescence (cross-) correlation spectroscopy in live cells and organisms. Nat. Protocols 10:1948-1974.
5. Bailey, K. A., and Z. D. Schultz. 2016. Tracking Bulk and Interfacial Diffusion Using Multiplex Coherent Anti-Stokes Raman Scattering Correlation Spectroscopy. The Journal of Physical Chemistry B 120:6819-6828.
6. Singh, A. P., J. W. Krieger, J. Buchholz, E. Charbon, J. Langowski, and T. Wohland. 2013. The performance of 2D array detectors for light sheet based fluorescence correlation spectroscopy. Opt. Express 21:8652-8668.
7. Perillo, E. P., Y.-L. Liu, K. Huynh, C. Liu, C.-K. Chou, M.-C. Hung, H.-C. Yeh, and A. K. Dunn. 2015. Deep and high-resolution three-dimensional tracking of single particles using nonlinear and multiplexed illumination. Nature communications 6.
8. Müller, C. B., K. Weiß, W. Richtering, A. Loman, and J. Enderlein. 2008. Calibrating Differential Interference Contrast Microscopy with dual-focus Fluorescence Correlation Spectroscopy. Optics express 16:4322-4329.
9. Stasevich, T. J., F. Mueller, A. Michelman-Ribeiro, T. Rosales, J. R. Knutson, and J. G. McNally. Cross-Validating FRAP and FCS to Quantify the Impact of Photobleaching on In Vivo Binding Estimates. Biophysical journal 99:3093-3101.
10. Capoulade, J., M. Wachsmuth, L. Hufnagel, and M. Knop. 2011. Quantitative fluorescence imaging of protein diffusion and interaction in living cells. Nat. Biotechnol 29:835-839.
11. Izeddin, I., V. Récamier, L. Bosanac, I. I. Cissé, L. Boudarene, C. Dugast-Darzacq, F. Proux, O. Bénichou, R. Voituriez, O. Bensaude, M. Dahan, and X. Darzacq. 2014. Single-molecule tracking in live cells reveals distinct target-search strategies of transcription factors in the nucleus. eLife 3:e02230.